A&A 576, A108 (2015)
DOI: 10.1051/0004-6361/201425004

Astronomy & Astrophysics

An *XMM-Newton* view of FeKα in high-mass X-ray binaries⋆

A. Giménez-García[1,4,6], J. M. Torrejón[1,2], W. Eikmann[3], S. Martínez-Núñez[2], L. M. Oskinova[4], J. J. Rodes-Roca[1,2,5], and G. Bernabéu[1,2]

[1] University Institute of Physics Applied to Sciences and Technologies, University of Alicante, PO Box 99, 03080 Alicante, Spain
e-mail: angelgimenez@ua.es
[2] X-ray Astronomy Group, Departamento de Física, Ingeniería de Sistemas y Teoría de la Señal, University of Alicante, PO Box 99, 03080 Alicante, Spain
[3] Dr. Karl Remeis-Sternwarte FAU Erlangen-Nürnberg, 96049 Bamberg, Germany
[4] Institute for Physics and Astronomy, University of Potsdam, 14476 Potsdam, Germany
[5] MAXI team, Institute of Physical and Chemical Research (RIKEN), 2-1 Hirosawa, Wako, 351-0198 Saitama, Japan
[6] School of Physics, Faculty of Science, Monash University, Clayton, VIC 3800, Australia

Received 16 September 2014 / Accepted 25 December 2014

ABSTRACT

We present a comprehensive analysis of the whole sample of available *XMM-Newton* observations of high-mass X-ray binaries (HMXBs) until August 2013, focusing on the FeKα emission line. This line is key to better understanding the physical properties of the material surrounding the X-ray source within a few stellar radii (the circumstellar medium). We collected observations from 46 HMXBs and detected FeKα in 21 of them. We used the standard classification of HMXBs to divide the sample into different groups. We find that (1) different classes of HMXBs display different qualitative behaviours in the FeKα spectral region. This is visible especially in SGXBs (showing ubiquitous Fe fluorescence but not recombination Fe lines) and in γ Cass analogues (showing both fluorescent and recombination Fe lines). (2) FeKα is centred at a mean value of 6.42 keV. Considering the instrumental and fits uncertainties, this value is compatible with ionization states that are lower than Fe XVIII. (3) The flux of the continuum is well correlated with the flux of the line, as expected. Eclipse observations show that the Fe fluorescence emission comes from an extended region surrounding the X-ray source. (4) We observe an inverse correlation between the X-ray luminosity and the equivalent width of FeKα (EW). This phenomenon is known as the X-ray Baldwin effect. (5) FeKα is narrow ($\sigma_{\rm line} < 0.15$ keV), reflecting that the reprocessing material does not move at high speeds. We attempt to explain the broadness of the line in terms of three possible broadening phenomena: line blending, Compton scattering, and Doppler shifts (with velocities of the reprocessing material $V \sim 1000$ km s^{-1}). (6) The equivalent hydrogen column ($N_{\rm H}$) directly correlates to the EW of FeKα, displaying clear similarities to numerical simulations. It highlights the strong link between the absorbing and the fluorescent matter. (7) The observed $N_{\rm H}$ in supergiant X-ray binaries (SGXBs) is in general higher than in supergiant fast X-ray transients (SFXTs). We suggest two possible explanations: different orbital configurations or a different interaction compact object – wind. (8) Finally, we analysed the sources IGR J16320-4751 and 4U 1700-37 in more detail, covering several orbital phases. The observed variation in $N_{\rm H}$ between phases is compatible with the absorption produced by the wind of their optical companions. The results clearly point to a very important contribution of the donor's wind in the FeKα emission and the absorption when the donor is a supergiant massive star.

Key words. surveys – X-rays: binaries – binaries: general – circumstellar matter – stars: winds, outflows – stars: early-type

1. Introduction

Since the early stages of X-ray astronomy, Fe lines in the spectral region of ∼6−7 keV (the Fe complex) have been studied in a large number of X-ray sources given its fruitfulness as a tool for plasma diagnostics. They were reported for the first time in the supernova remnant Cas A (Serlemitsos et al. 1973), and only two years later in a high-mass X-ray binary (HMXB) using the Ariel 5 satellite (Sanford et al. 1975). The most recent X-ray space missions (*Swift, Suzaku, Chandra*, and *XMM-Newton*) have triggered a notable improvement in the attainable spectral resolution and effective area, permitting between different emission features in the Fe complex to be distinguished: narrow and broad fluorescence lines (FeKα and FeKβ), Compton shoulders and recombination lines (Fe XXV and Fe XXVI; Torrejón et al. 2010b). This improvement has given a remarkable impetus to the study of the Fe complex, and it justifies a comprehensive analysis in HMXBs.

In particular, FeKα has been proven to be a fundamental tool in the study of HMXBs (Martínez-Núñez et al. 2014; Rodes-Roca et al. 2011; van der Meer et al. 2005). The origin of the fluorescence-emitting region has been discussed by many authors in the past. Nagase (1989) considered accretion disks and the matter stagnated in the accretion and ionization wakes in the stellar wind as plausible areas of FeKα production. Watanabe et al. (2006) analysed the classical HMXB Vela X-1 and proposed the extended stellar wind, reflection off the stellar photosphere, and an accretion wake as the most likely candidates for fluorescence-reprocessing regions. In any case, FeKα is very sensitive to the physical conditions of the vicinity of the X-ray source, so it provides remarkable information that must be analysed.

Fluorescence is produced as a consequence of the X-ray illumination of matter. When an Fe atom absorbs a photon carrying sufficient energy to remove an electron from its K-shell ($E > 7.2$ keV), the vacancy can be occupied by another electron from an outer shell. If the electron comes from the L-shell, the transition produces FeKα emission. This emission is produced

⋆ Appendices are available in electronic form at http://www.aanda.org

when the vacancy is filled by a former M-shell electron. When Fe is more ionized than Fe XIX, the fluorescence yield starts to decrease with the ionization state (Kallman et al. 2004). Therefore, FeKα is a footprint of not extremely ionized Fe (less than Fe XX). On the other hand, recombination lines Fe XXV and Fe XXVI unveil the presence of very hot gas, where Fe atoms are almost completely stripped.

Previous comprehensive surveys of the Fe complex in HMXBs were carried out by Gottwald et al. (1995) using EXOSAT and Torrejón et al. (2010b) using the High-Energy Transmission Gratings (HETGS) onboard *Chandra*. The high spectral resolution provided by *Chandra* gratings proved to be instrumental in disentangling the different ionization species present in the Fe complex. However, the relatively low throughput of the instrument only allowed studying the brightest binaries. In this study we increase the previous sample significantly by using the high throughput of *XMM-Newton* EPN. This has allowed us to include fainter systems (such as Be X-ray binaries (BeXBs) or SFXTs in quiescence), while the moderate resolution of the EPN CCDs has allowed us to test previous correlations based on a small sample.

HMXBs are especially susceptible to being studied using the Fe complex, on account of the significance of the circumstellar medium in the observable phenomena. These systems consist of a compact object, either a neutron star (NS) or a black hole (BH), accreting matter from a massive OB star (usually called the optical or normal star of the system). In HMXBs, the observed luminosity is commonly powered via accretion. Consequently, the way that matter is accreted from the donor directly defines the observable luminosity features of each source.

When the optical star is a Be star, the system is a BeXB. Be stars are fast-rotating BIII-V stars that have shown spectral emission lines at some point in their lives. They also show an excess of infrared emission, when they are compared to non Be stars of the same spectral type. These observables are explained by appealing to an extended circumstellar decretion disk. BeXBs are usually transient in the X-rays, although some systems exhibit a persistent quiescence emission ($L \leq 10^{34-35}$ erg/s). The outbursts have been traditionally classified in two types. Type-I outbursts ($L \leq 10^{37}$ erg/s) are related to periastron passages. Type-II outbursts are not related to the orbital phase and imply an even higher increase in luminosity than Type-I outbursts, reaching the Eddington luminosity (for a review on BeXBs see Reig 2011).

In the case of classical supergiant X-ray binaries (SGXBs), the compact object is embedded in the dense and powerful wind of a OB supergiant companion, swallowing everything that enters its gravitational domain. The mass loss rate of the donor is $\gtrsim 10^{-7}\,M_{\odot}\,\mathrm{yr}^{-1}$, and the compact object is usually found at a close distance of $\sim 1.5-2\,R_{\star}$. In such a close orbit, the captured matter is able to fuel a persistent X-ray emission of $\sim 10^{33-39}$ erg/s. Flares and off-states are often observed in SGXBs, indicating an abrupt transition in the accretion rate. They might be produced either by sudden variations in density in the medium transited by the compact object (Martínez-Núñez et al. 2014; Kreykenbohm et al. 2008) or by instabilities above the magnetosphere of the neutron star, as proposed in the quasi-spherical accretion theory by Shakura et al. (2012).

The medium transited by the compact object through the extended atmosphere of an OB supergiant star is not smooth because of at least two phenomena. First, density inhomogeneities (clumps) are present as an intrinsic feature of the radiatively driven winds of hot stars (Lucy & White 1980; Oskinova et al. 2012). Second, hydrodynamical simulations show that the X-ray radiation and the gravity field of the compact object disturb the wind of the donor, inducing the formation of denser structures such as filaments, bow shocks, and wakes (Blondin et al. 1990, 1991).

In the past decade and a half, new discoveries have led to the addition of new groups to the previous picture of HMXBs, stressing the value of grasping the different features of the sources such as geometry, compact object properties, optical star peculiarities, and wind clumpiness. The new groups are supergiant fast X-ray transient systems (SFXTs), γ Cassiopeae analogues, and γ-ray binaries.

SFXTs are systems with a supergiant optical star, as in SGXBs, but they are defined by extremely transient behaviour. During quiescence they exhibit low luminosity ($\sim 10^{32}$ erg/s), but they spend most of their time at an intermediate level of emission ($\sim 10^{33-34}$ erg/s). They display short outbursts (~few hours), reaching luminosities up to 10^{36-37} erg/s (Sidoli et al. 2009). It is likely that the clumpiness of the wind plays a main role in the variability of these sources. Other mechanisms involving centrifugal and magnetic barriers could enhance the observed luminosity swings, thereby relaxing the needed variation amplitudes in the physical conditions of the wind (Bozzo et al. 2008). Nevertheless, other authors explain the variability appealing to the quasi-spherical accretion model (Drave et al. 2013; Paizis & Sidoli 2014).

The γ Cassiopeae analogues are characterized by the thermal nature of the X-ray emission, with plasma temperatures of $\sim 10^{8}$ K (~10 keV), an X-ray luminosity of 10^{32-33} erg/s, and high flux variability on various time scales. However, they do not display giant outbursts as observed in BeXBs (Lopes de Oliveira et al. 2010). Presently, it is not clear that the X-ray emission is emitted by accretion processes (onto a neutron star or a white dwarf) or, alternatively, generated from the interaction between the surface of the star, the circumstellar disk, and its magnetic field.

High-mass γ-ray binary systems (HMGBs) are HMXBs where the emission peaks above 1 MeV. Nowadays, it is thought that the emission is caused by accelerated particles in the shock that is produced when the pulsar wind collides the massive star wind. Therefore, they are powered by the rotational energy of the neutron star, in opposition to the rest of HMXBs, which are accretion fed. There are currently five confirmed HMGBs, all of them with a main sequence optical star (for a review on HMGBs see Dubus 2013).

Finally, there are sources that, for a number of reasons, cannot be classified in any of the already mentioned classes of HMXBs. Particularly, among the set of sources studied in this paper, they are 4U 2206+54, Centaurus X-3, and Cygnus X-1. The optical star in 4U 2206+54 is a O9.5V (Blay et al. 2006), which is neither a supergiant nor a Be star. The system may be part of a new group of wind-fed HMXBs with a main sequence donor (Ribó et al. 2006). Centaurus X-3 and Cygnus X-1 are the only systems here that were collected where accretion is persistently driven by an accretion disk (Tjemkes et al. 1986; Shapiro et al. 1976), which is reflected in the spectra of both sources.

In this paper, we study the FeKα line for the whole sample of HMXBs available with *XMM-Newton* until August 2013. In Sect. 2 we present the set of observations, the reduction process and the more important details concerning the spectral fits. In Sect. 3 we show our results: a spectral atlas that includes every fit and different plots relating fit parameters. In Sect. 4 we interpret the obtained results and summarize the most important conclusions in Sect. 5. In Appendix A we present a set of tables that describe the obtained parameters from the spectral fits. In

Appendix B we show the spectral atlas, which contains the plot of every spectrum that we have analysed in this survey. We show the observations and the models, together with the ratio between them.

2. Observations and data treatment

The *XMM-Newton* observatory (Lumb et al. 2012) is fitted with three X-ray telescopes of 1500 cm^2 and a coalignated optical telescope. Spectroscopy and photometry are done by the six instruments on board: three X-ray imaging cameras EPIC (European Photon Imaging Camera), two grating X-ray spectrometers RGS (Reflection Grating Spectrometer), and an optical monitor (OM). EPIC cameras (0.1−15 keV) are the only instruments at *XMM-Newton* that cover the energy range of the Fe complex. Among EPIC, one camera uses PN CCDs, and the other two use MOS CCDs. EPIC PN cameras (EPN) surpass the effective area of the MOS cameras at 6−7 keV by a factor ∼3, making EPN more suitable for our purposes. Compared to other missions, the HETGS onboard *Chandra* provides better energy resolution in the energy range of the Fe complex, but the effective area available with EPN is significantly higher. EPN provides the adequate conditions for performing the study presented here, on account of the moderate (but sufficient) spectral resolution ($\Delta E/E \sim 40$) and large effective area (∼1000 cm^2), enabling us to analyse a large amount of sources in a homogeneous and consistent way.

Since HMXBs are usually variable, we often observe a dramatic change in luminosity even in the same observation, thus remarkably affecting the spectral parameters. In these cases, an averaged spectrum does not reproduce the actual emission of the source, and it is advisable to split the observation into more than one time interval. We have considered five different states[1] of the systems in order to define the time intervals: dips, quiescence, flares, eclipse ingress/egress, and eclipse. We used the following criteria. When luminosity drops a factor ≳2 on the timescale of ≲1 h, we tagged the time interval as a dip. Analogously, when luminosity rises ≳2 on the timescale of ≲1 h, we labelled the time interval as a flare. For observations covering eclipsing phases, we defined time intervals for eclipse ingress/egress and eclipse. The rest of time intervals are tagged as quiescent states.

In Fig. 1 we see the light curve of an observation of 4U 1538-522 as an example of how we have split the time intervals in the observations. The source was observed during the ingress in an X-ray eclipse, which is clearly noticeable in the light curve. We separated the observation into two time intervals, one covering the ingress in eclipse and another one covering the eclipse.

In summary, we have collected data from 46 HMXBs. Twenty-one of them exhibit FeKα emission. We note that some sources have more than one available observation. Taking everything into account (46 sources, temporal splitting depending on the state of the source, and more than one observation per source in some cases), we end up with a total number of 108 spectra that we have analysed.

We followed the catalogue of Liu et al. (2006), in addition to later discoveries or confirmations, to identify the currently known HMXBs, and used every available *XMM-Newton* public observation[2]. The sources not included in the Liu catalogue, but considered here are HD 119682, SS 397, IGR J16328-4726, HD 45314, HD 157832, Swift J045106.8-694803, IGR J16207-5129, and XTE J1743-363.

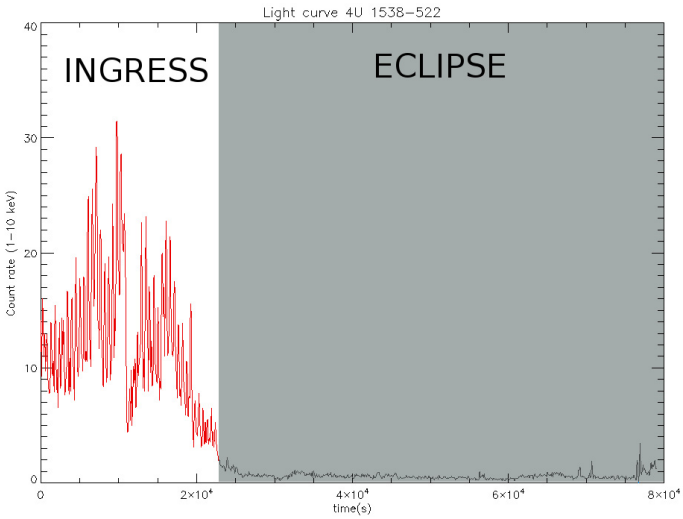

Fig. 1. Light curve of the observation of 4U 1538-522 (ObsID:0152780201). We have split the observation in two parts, one for the ingress in the eclipse and another one for the eclipse.

2.1. Data reduction

We have reduced the data using Science Analysis System (SAS), version 12.0.1. Since the sample of observations contain a heterogenous group of HMXBs, we found different observation modes (timing and imaging) to account for the different properties of the sources. In the brightest systems, the observations were usually performed using the timing mode, while the faintest sources were observed using imaging modes.

Timing modes permit the arrival of photons to be processed at a high rate, since only one CCD operates, and the information is collapsed into one dimension, allowing a fast read out. The time resolution is as high as 30 μs (7 μs in burst mode; Kirsch et al. 2006). Even with the high timing resolution reached with these observation modes, pile-up is still present in several cases, especially when the count rate is ≳800 counts s^{-1}. We checked in every observation whether pile-up is affecting the data, using the SAS task *epatplot*, and we excised the core of the source's point spread function in the pertinent cases. The size of the excised region has been chosen wide enough to remove the unwanted pile-up effects (see examples of the use of *epatplot* in Ng et al. 2010).

The background-subtraction process also depends on the brightness of the source. In the EPN timing mode, the PSF of the sources displaying ≳200 counts s^{-1} will span the whole CCD. Therefore, any area selected as a background region will be contaminated by source photons. Since this effect is strongly energy dependent, for the brightest sources we have chosen a method of background subtraction that is similar to the one performed in the analysis of Vela X-1 by Martínez-Núñez et al. (2014), where a blank sky spectrum taken in timing mode is used as the real background for energies below 2.5 keV, while the rest of the spectrum corresponds to the outermost pixels of the CCD. Meanwhile, for common observations, we have used source-free regions to extract a background spectrum and subtract it from the former source plus background energy distribution.

[1] The states considered in this work and those also called states in black hole binary systems must not be confused.

[2] http://xmm.esac.esa.int/xsa/

Table 1. List of models used to fit the continuum, described in XSPEC notation.

	Model	Continuum models
Non-thermal	N_1	$powerlaw \times tbnew \times cabs$
	N_2	$powerlaw_1 \times tbnew_1 \times cabs_1 + powerlaw_2 \times tbnew_2 \times cabs_2$
	N_3	$powerlaw_1 \times tbnew_1 \times cabs_1 + powerlaw_2 \times tbnew_2 \times cabs_2 + powerlaw_3 \times tbnew_3 \times cabs_3$
Thermal	T_1	$mekal \times tbnew \times cabs$
	T_2	$(mekal + mekal) \times tbnew \times cabs$
	T_3	$(mekal + mekal + mekal) \times tbnew \times cabs$
	T_4	$(cemekl) \times tbnew \times cabs$
	T_5	$bbody \times tbnew \times cabs$
	T_6	$(bbody + bbody) \times tbnew \times cabs$
	T_7	$(bbody_1 + bbody_2) \times tbnew \times cabs$
	T_8	$bbody_1 \times tbnew_1 \times cabs_1 + bbody_2 \times tbnew_2 \times cabs_2$
	T_9	$diskbb \times tbnew \times cabs$
	T_{10}	$(diskbb + bbody) \times tbnew \times cabs$
	T_{11}	$bremss \times tbnew \times cabs$
	T_{12}	$bbody \times tbnew \times cabs + bremss \times tbnew \times cabs$
	T_{13}	$(bremss + bbody) \times tbnew \times cabs$
Both	TN_1	$(powerlaw + bbody) \times tbnew \times cabs$
	TN_2	$powerlaw \times tbnew_1 \times cabs_1 + bbody \times tbnew_2 \times cabs_2$
	TN_3	$(powerlaw + diskbb) \times tbnew \times cabs$
	TN_4	$powerlaw \times tbnew_1 \times cabs_1 + diskbb \times tbnew_2 \times cabs_2$
	TN_5	$(powerlaw + mekal) \times tbnew \times cabs$

Notes. The basic components are *powerlaw, bbody, diskbb, bremss, mekal*, and *cemekl*, together with *tbnew*, to account for the absorption and *cabs* for the non-relativistic Compton scattering. The employed models are a combination of these components, in addition to Gaussian profiles modelling emission lines. We divide the models into three types: $N_\#$ for non-thermal, $T_\#$ for thermal, and $TN_\#$ for models containing both thermal and non-thermal components.

Ancillary response files were generated using the SAS task *arfgen*. For observations taken in timing mode affected by pile-up, we followed the recommendations of the *XMM-Newton SAS User Guide* in order to generate the appropriate ancillary response files. Response matrices were created using the SAS task *rmfgen*.

2.2. Spectral fitting

For the spectral analysis we used XSPEC, version 12.8.0[3]. We rebinned the spectra to have a minimum of 20 counts per bin and a bin size of at least one-third of the FWHM of the intrinsic energy resolution, in order to be allowed to apply χ^2 statistics in the fitting of a set of Poissonian data (Cash 1979).

In Table 1 we present the sample of models employed for the continuum in the fits. Every model is a combination of additive and multiplicative models. An additive model stands for a source of X-rays (e.g. bremsstrahlung radiation), and a multiplicative model represents an energy-dependent change of an additive model (e.g. photoelectric absorption).

The models presented in Table 1 were tested in every observation and accepted depending on the reduced-χ^2 ($\frac{\chi^2}{n-m}$, with n the number of bins and m the number of fitted parameters). Each observation has particular characteristics, and therefore the decision of which reduced-χ^2 value is acceptable has been taken one by one. In Fig. 2 we can see that most of the fits result in a reduced-$\chi^2 \simeq 1$, as expected for a suitable fit. The highest value of reduced-χ^2 for an accepted model has been 1.82. The parameters arising from the fits are listed in Tables A.2 and A.3.

We can classify the additive components of the models as thermal or non-thermal. A component is called thermal when radiation is produced as a consequence of the thermal motion of the plasma particles (e.g. blackbody radiation). Otherwise, the emitted radiation is non-thermal (e.g. non-thermal inverse-Compton emission). If all the additive components of a model are thermal, we classify the model as thermal (analogously for non-thermal). We also used hybrid models, combining thermal and non-thermal components. The thermal components used in this work are the following:

- *bbody*: blackbody emission;
- *diskbb*: model of an accretion disk emission made of multiple blackbody components;
- *bremss*: thermal bremsstrahlung emission (electrons distributed according to the Maxwell-Boltzmann distribution);
- *mekal*: emission from optically thin hot gas, including spectral lines from several elements (Mewe et al. 1985);
- *cemekl*: built from the mekal model, incorporating multi-temperature emission.

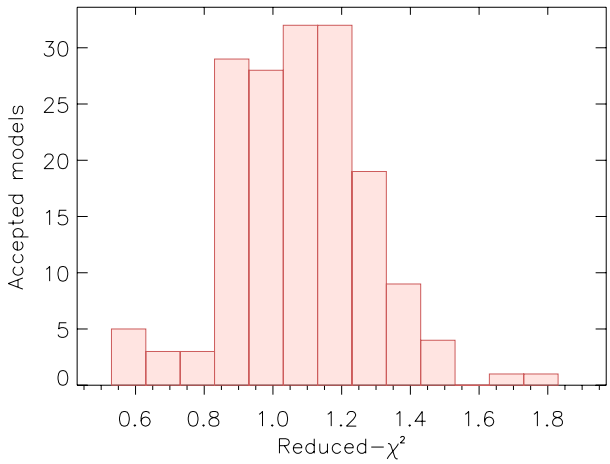

Fig. 2. Number of accepted models depending on the reduced-χ^2 value.

[3] http://heasarc.nasa.gov/xanadu/xspec/

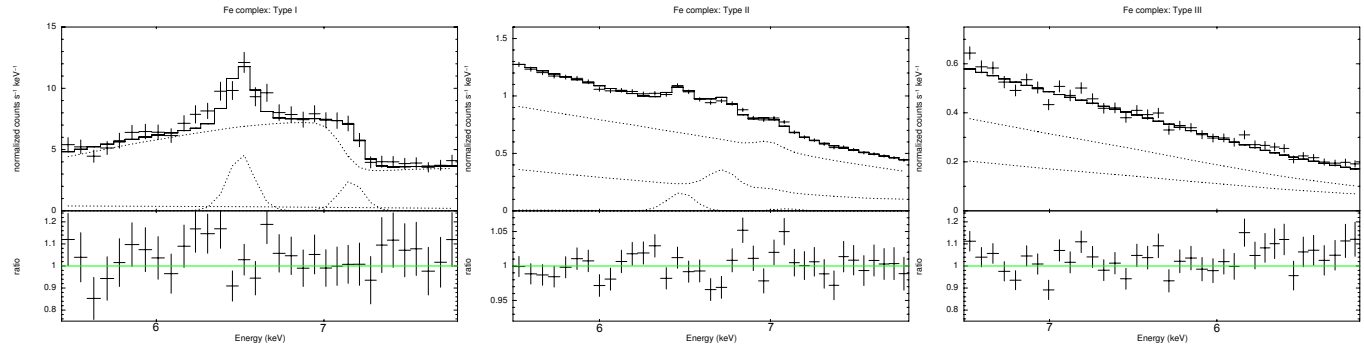

Fig. 3. Patterns found in the Fe complex of HMXBs: Type I (*left panel*), Type II (*central panel*), and Type III (*right panel*).

On the other hand, the only non-thermal component used in this work is:

– *powerlaw*: phenomenological model consisting of a simple inverse power law profile ($\propto E^{-\Gamma}$). This profile is a footprint of inverse-Compton scattering by hot electrons (non-thermally distributed) of a seed radiation field.

For the photoelectric absorption, we used *tbnew*[4], the improved version of the Wilms et al. (2000) model *tbabs*, setting the cross sections to the Verner et al. (1996) ones and the abundances according to Wilms et al. (2000). The most important parameter of this model is the total equivalent hydrogen column $N_{\rm H}$, which is the integrated amount of hydrogen atoms in the line of sight from the observer to the source, per cm^2. We also added the model *cabs* to account for the Compton scattering, which is not comprised in the *tbnew* model and is especially significant for $N_{\rm H} \gtrsim 10^{24}$ cm^{-2}.

The emission lines are fitted using Gaussian profiles. We have categorized any emission line that fulfils the following conditions as FeKα:

1) The centroid energy of the Gaussian component lies in the interval [6.3, 6.65] keV. The interval includes the expected energy of FeKα emission from Fe II (~6.395 keV) to Fe XXIII (~6.63 keV) (Kallman et al. 2004). This condition excludes the detection of any hypothetical fluorescent emission from Fe XXIV-XXV at ~6.67−6.7 keV, thereby excluding any confusion between FeKα and the recombination line Fe XXV at similar wavelength. The fluorescence yields of Fe XXIV-XXV are low compared to lower ionization states.
2) The statistical significance ($\sigma_{\rm sign}$) of the Gaussian component is greater than 2σ. We calculated $\sigma_{\rm sign}$ from $\chi^2_{k_1} - \chi^2_{k_2}$, assuming $\chi^2_{k_1} - \chi^2_{k_2} \sim \chi^2_{k_1-k_2}$[5], where $\chi^2_{k_1}$ arises from a fit using certain model with the Gaussian component included, and $\chi^2_{k_2}$ arising from a fit using the same model without the Gaussian component.

In some cases, FeKα line is clearly noticeable, but FeKβ is not prominent enough to permit erroneous estimation of its parameters. In these cases, we have constrained the centroid energy and the norm of FeKβ according to Kallman et al. (2004):

– Energy(FeKβ) = Energy(FeKα) + 0.652 keV.
– Norm(FeKβ) = Norm(FeKα) × 0.13 photons/cm^2/s.

[4] http://pulsar.sternwarte.uni-erlangen.de/wilms/research/tbabs/

[5] This assumption is not strictly true, since $\chi^2_{k_1}$ and $\chi^2_{k_2}$ are not independent. However, it provides an estimation of the impact of the Gaussian component in the model.

The estimated parameters, like the EW, are very sensitive to the fit of the continuum. Therefore, although the Fe complex appears in the ~6−7 keV energies, we broadened the spectral scope to an energy range of 1−10 keV to perform the analysis. It also allows us to consider possible calibration inaccuracies in the charge transfer inefficiency (CTI) and the X-ray loading (XRL), an issue reported in previous analysis of EPN observations (see Martínez-Núñez et al. 2014; Fürst et al. 2011). In the few cases of possible CTI or XRL, we applied an artificial gain $E_{\rm new} = \frac{E_{\rm old}}{\rm slope}$ + offset (see Table A.2).

The estimation of the parameter confidence regions (at 90% level) have been calculated with a Markov Chain Monte Carlo (MCMC) technique, implemented in XSPEC, where N generations of the set of free parameters are used to determine the best-fit values and the confidence regions. We set $N = 1.5 \times 10^4$ in our calculations. These chains are also valid for estimating fluxes and equivalent widths.

3. Results

3.1. Spectral atlas

In Appendix B, we present the full sample of analysed spectra. The figures in Appendix B show the set of analysed observations (cross points), the model employed (solid line), the components of the model (dotted line), and the ratio between observation and model (lower box in each spectrum plot).

We show a list of the sources in Table A.1, giving the class where we have grouped them and the reference for such a classification. We can see that the different classes of HMXBs behave qualitatively differently in the region of the Fe complex (~6−7 keV), reflecting the distinct accretion regimes that characterize them. We have observed three patterns in the Fe complex, which we define as Types I, II, and III (see Fig. 3). We define Type I, when fluorescence lines FeKα and FeKβ are observed, but not recombination lines Fe XXV and Fe XXVI. We define Type II, when fluorescence lines are detected, together with recombination lines Fe XXV and Fe XXVI. Finally, we define Type III, when Fe lines are not detected.

The general features observed in this work for the different groups of HMXB are summarized in Table 2, and explained below in more details:

– BeXBs. We collected data from ten sources. All the observations were performed in quiescence. We have detected FeKα emission in only one BeXB (SAX J2103.5+4545). The upper limit of the FeKα EW in the rest of BeXBs is in general higher than the observed value in SAX J2103.5+4545, implying that the lack of detections might be due to a poor signal-to-noise. The spectra can be

Table 2. Description of the features observed in this work for the different groups of HMXBs.

Group	# Sources	Fe complex	Models	$N_{\rm H}$
BeXB	10	Type III	T, TN	Low
SGXB	12	Type I	N	High
SFXT	10	Type III (in quiescence)	T, N, TN	High
γ Cass like	8	Type II	T	Low
HMGB	2	Type III	T, N, TN	Low

Notes. We have analyzed data of 46 sources. However, those classified as peculiars (3 sources) or unclassified (AX J1749.1-2733) are not included in this table. We define $N_{\rm H}$ of a group as high, when the typical value observed is well over the estimations of the interstellar $N_{\rm H}$ in the line of sight of the sources following Willingale et al. (2013). That is, we say that the $N_{\rm H}$ of a group is high when the absorption is typically intrinsic to the systems.

modelled by thermal or a combination of thermal and non-thermal components, except for Swift J045106.8-694803 (fitted using an absorbed power law). Seven sources accept a thermal model, and six a combination model (4 of them accept both).

– SGXBs. We have gathered data from 12 sources. Ten of them show detectable Fe fluorescence emission. The only exceptions are IGR J16465-4507 and SAX J1802.7-2017, the most distant SGXBs included in this work, at 12.5 and 12.4 kpc, respectively. The EW upper limits in these two sources are high, implying that their faintness is very likely the reason we do not detect FeKα. The 12 SGXBs can be well fitted using non-thermal models, although thermal components are also plausible in some sources. In general, SGXBs are characterized by high absorption and the presence of Fe fluorescence emission lines.
– SFXTs. We have collected data from ten sources. Three of them show FeKα: AX J1841.0-0536, IGR J11215-5952, and IGR J16479-4514. The EW upper limit in the rest of sources is high. Therefore, FeKα would probably be detectable with a better signal-to-noise. The models employed for fitting the SFXT systems are very heterogeneous, with no preference for thermal or non-thermal, or for a combination of both kinds of models.
– γ Cassiopeae analogues. We have gathered observations from eight sources. Five of them exhibit FeKα. The EW upper limit in the three other sources is very high. Again, it implies a very likely presence of fluorescence in the case of better signal-to-noise. In addition, recombination lines of Fe XXV and Fe XXVI are always present in the set of γ Cassiopeae analogues. These lines are included in the XSPEC model *mekal*. For most of the observations we have achieved a good fit using a combination of *mekal* components. In a few cases we used other components: *diskbb* and *powerlaw*, but *mekal* is by far the one employed most in γ Cassiopeae-like systems, in agreement with previous X-ray analyses (Lopes de Oliveira et al. 2010, 2006).
– HMGBs. We collected data from two HMGBs: LS I+61 303 and LS 5039. None of them show Fe features. However, the signal-to-noise in these observations is poor and the upper limits of the FeKα EW are high enough to not rule out the presence of the line. We have used both thermal and non-thermal components in the fits.
– Peculiars. These are a set of sources that do not fit into any of the aforementioned classes of HMXBs, as explained in the introduction. We collected data from three such systems: 4U 2206+54, Centaurus X-3, and Cygnus X-1:
  – 4U 2206+54 does not show any detectable Fe emission line, and the upper limit in the EW of FeKα is low (comparable to the upper limits in the BeXBs). It can be fitted by means of an hybrid model (thermal plus non-thermal components).
  – Centaurus X-3 presents a rich emission-line spectrum. Concretely, in the Fe complex we are able to identify FeKα, FeKβ, Fe XXV, and Fe XXVI. We used either an hybrid model either a non-thermal model.
  – Cygnus X-1 exhibits a broad Fe feature, sometimes combined with a faint and narrow, but statistically significant, FeKα line. We have mostly used non-thermal models, occasionally combined with a *bbody* or a *diskbb* component.
– AX J1749.1-2733. In this system, the optical member has been classified as a B1-2 (Karasev et al. 2010), but the luminosity class remains unknown, preventing us to incorporate the source in a defined group. Although it does not exhibit detectable Fe emission, the high absorption clearly points to a supergiant companion. In addition, the EW upper limit of FeKα is compatible with the values observed in SGXBs and SFXTs. It can be well fitted using an absorbed *powerlaw* or a *blackbody*.

In summary, it is very likely that FeKα is a ubiquitous feature in HMXBs, and its detection strongly depends on the quality of the observations. In this regard, the EW of the line is very affected by the level of intrinsic absorption present on the sources (see also Sect. 3.4.3). SGXBs and SFXTs, which show higher absorption, tend to exhibit a more prominent Fe fluorescence.

3.2. FeKα width

In Table A.3 we show the parameters of every detected FeKα, including the width of the line ($\sigma_{\rm line}$). We made a distinction between narrow and broad FeKα. We defined narrow FeKα as when $\sigma_{\rm line} < 0.15$ keV, and broad FeKα as when $\sigma_{\rm line} > 0.15$ keV. This separation is both physically and observationally motivated.

The origin of broad Fe features in X-ray binaries is still an open question, but the most likely alternatives are related to the presence of an accretion disk (see e.g. Hanke et al. 2009; Ng et al. 2010; Duro et al. 2011). However, narrow features are not compatible with material rotating at high velocities or being relativistically broadened. Given that broad and narrow FeKα have clearly different origins, they must be analysed in different ways. Then, it raises the question of how to define the separation mark between them. In Fig. 4 we can see that in our sample the number of detected sources decreases when increasing $\sigma_{\rm line}$. Moreover, most of the detections are grouped at $\sigma_{\rm line} < 0.15$ keV. As a result, $\sigma_{\rm line} < 0.15$ keV seems a natural threshold for the definition of narrow lines in the sample. In addition, we must pay attention to the plausible contamination of FeKα with Fe XXV, which is located at ~6.7 keV. The chosen criterion separates the sources where it is very unlikely that FeKα is contaminated by Fe XXV (narrow lines), from the sources that probably suffer from this problem (broad lines). A more detailed analysis of broad Fe features in HMXBs is beyond the scope of this paper and it will be discussed fully in a forthcoming work.

Hereafter, when FeKα is mentioned, we refer to the narrow feature. From the total number of 108 analysed observations we find detected (narrow) FeKα in 60 of them.

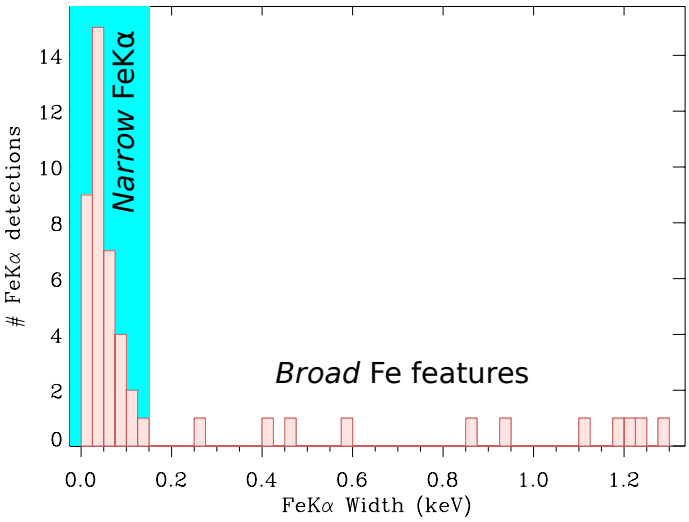

Fig. 4. Histogram of the FeKα width. The bulk of the detections are grouped showing $\sigma_{\rm line} < 0.15$ keV. We define them as narrow FeKα. The rest are defined as broad Fe features. Even though we have detected 60 narrow FeKα, this plot only includes 38. The reason is that 22 of them are very narrow (or the signal-to-noise very low) and they have been treated in the fits as delta functions. (In Table A.3 we present their width as $\sigma_{\rm line} = 0$.)

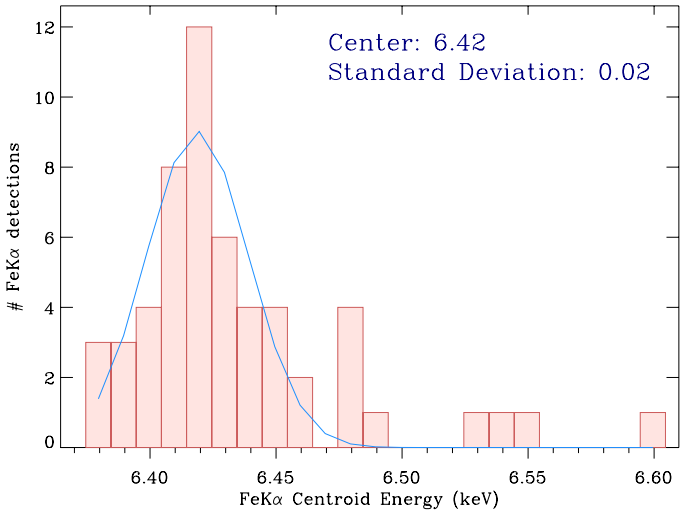

Fig. 5. Centroid energy of FeKα with a Gaussian fit overplotted (blue profile). The mean value is 6.42 ± 0.02 keV, compatible with Fe I-XVIII. Even though we have 60 detections of FeKα, in this plot we only see 55. Five cases fulfil the requirements of detection, but the low signal-to-noise rations do not permit finding an accurate centroid energy. They have not been included in this plot. In these five cases we set the centroid energy of FeKα to ~6.4 keV.

3.3. Centroid energy

In Fig. 5 we can see a histogram that presents the centroid energy of FeKα. A Gaussian fit of the data reveals a mean value for the centroid energy of 6.42 keV. There are no significant differences in the averaged values obtained for different classes of HMXBs or for different states. The standard deviation is 0.02 keV, comparable to the error that we typically obtain in the estimation of the centroid energy in the fits (see Table A.3). After taking the standard deviation and the uncertainties in the CTI corrections in EPN[6] into account, the centroid energy of FeKα constrains the ionization state of Fe to less ionized than Fe XVIII (Kallman et al. 2004), in agreement with previous studies in HMXBs (Torrejón et al. 2010b; Gottwald et al. 1995; Nagase 1989). In this regard, the study of Torrejón et al. (2010b) using HETGS (more accurate in wavelength than EPN) gives a narrower constraint on the ionization state (Fe I-X). Our present work supports this result and adds more sources to the sample.

On the right-hand side of Fig. 5 we can see seven FeKα detections emerging from the Gaussian profile. Four of them are unlikely to be described by such a Gaussian profile, since they lie more than three times the standard deviation away from the mean energy. All four belong to Cygnus X-1.

3.4. Correlated parameters

One of the goals of this work is to study plausible correlations that involve the parameters of FeKα (position, width, intensity, and EW, and other parameters in the fits, such as the absorbing column and the intensity of the continuum. Even when a good fit is reached, the confidence region of a parameter might be occasionally difficult to find owing to the dependence of the parameter on other parameters of the model. In each of the following sections, we specify the number of cases where a successful estimation of the 90% confidence region has been done.

[6] Please find more information about long-term CTI correction in the release note *EPIC-pn Long-Term CTI*, by M.J.S Smith et al. (2014), at http://xmm2.esac.esa.int/docs/documents/CAL-SRN-0309-1-0.ps.gz; and *EPIC status of calibration and data analysis* by Guainazzi (2008), at http://xmm2.esac.esa.int/external/xmm_sw_cal/calib/CAL-TN-0018.pdf

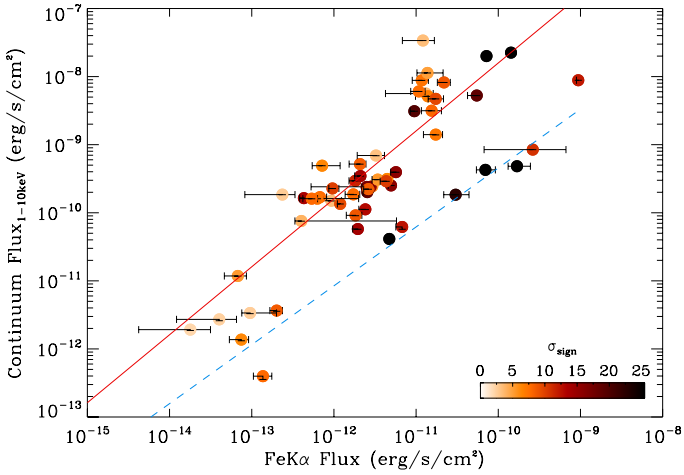

Fig. 6. $F_{1-10\ \rm keV}$ versus $F_{\rm FeK\alpha}$. Blue dashed line marks the correlation observed for IGR J16318-4848 jointly with eclipse observations, and the red solid line follows the bulk of the observations. The colour map indicates the $\sigma_{\rm sign}$ of the line (defined in Sect. 2.2).

3.4.1. Continuum flux vs. FeKα flux

In Fig. 6 we represent the unabsorbed flux of the continuum between 1–10 keV cancelling FeKα emission ($F_{1-10\ \rm keV}$), against the flux of FeKα ($F_{\rm FeK\alpha}$). We have successfully found a 90% confidence region of the flux of FeKα in 56 cases.

On a logarithmic scale, we identify two different patterns of correlation. First, for a subset including all the eclipse observations and IGR J16318-4848, we find a correlation with Pearson coefficient (PC) of 0.98. Second, for the rest of the observations, we find a correlation with PC = 0.89.

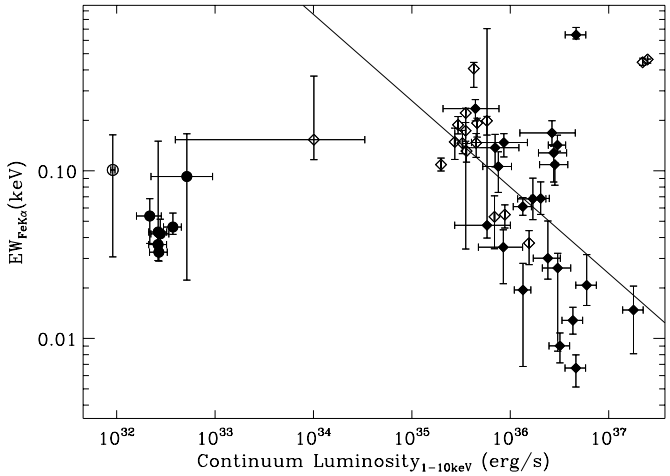

Fig. 7. EW of FeKα against $L_{1-10\ \rm keV}$. γ Cassiopeae analogues (circles) lie at $L_{1-10\ \rm keV} < 10^{33}$ erg/s. Open symbols indicate that either the distance or the error in the estimation of the distance is unknown. The solid line corresponds to a linear fit on logarithmic scale of the filled diamonds, that is, the sources with available distance with error estimation and $L_{1-10\ \rm keV} > 10^{33}$ erg/s.

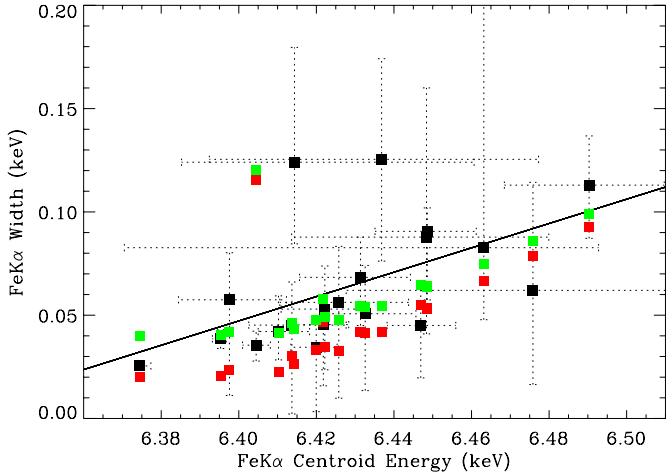

Fig. 8. Width of FeKα ($\sigma_{\rm line}$) versus the centroid energy (black squares). The black solid line traces a linear fit. We have marked in colour the expected width from the contribution of three different broadening phenomena: line blending, Compton broadening, and Doppler shifts, considering velocities of $V(\rm km\,s^{-1})$ = 1000 (red) and $V(\rm km\,s^{-1})$ = 2000 (green). Every single black square has an associated single red square and a single green square corresponding to the expected values of $\sigma_{\rm line}$ for that observation (see Sect. 4).

A linear fit of the parameters (on logarithmic scale) in the out-of-eclipse observations (Fig. 6) gives the following dependence:

$$F_{1-10\ \rm keV}(\rm erg/s/cm^2) = F_{\rm FeK\alpha}^{1.00\pm0.08}(\rm erg/s/cm^2) \times 10^{2.18\pm0.87}. \quad (1)$$

The errors show the standard deviation of the parameters in the linear fit.

The observed divergence amongst eclipse (plus IGR J16318-4848) and out-of-eclipse observations suggests that the companion star blocks the continuum and the FeKα emission in different proportions. Therefore, an important contribution of the fluorescence emission is produced in an extended region of $R \gtrsim R_\star$. This is consistent with previous analysis of eclipse observations of HMXBs (e.g. Rodes-Roca et al. 2011; Audley et al. 2006). In particular, Audley et al. (2006) estimate that 20% of FeKα in OAO 1657-415 is emitted from 19 light seconds off the X-ray source.

We also have the luminosity of the continuum to compare with the EW of FeKα. For the flux-to-luminosity conversion, we used the estimations of the distance shown in Table A.1. We have excluded eclipse and IGR J16318-4848 from this analysis, given that the EW is strongly affected by the high obscuration of the continuum that they suffer from. In Fig. 7 we plot the EW of FeKα against the unabsorbed luminosity of the continuum between 1−10 keV cancelling FeKα emission ($L_{1-10\ \rm keV}$). We observe two different groups of sources: 1) γ Cassiopeae analogues lying at low luminosities ($L_{1-10\ \rm keV} < 10^{33}$ erg/s); 2) the rest of sources that exhibit FeKα. The γ Cassiopeae analogues do not show any evident correlation (there are very few points), while the rest present a moderate inverse correlation (PC = −0.25, and PC = −0.39 using only the sources with an available estimation of distance with error, marked as filled diamonds in Fig. 7). A linear fit in Fig. 7 leads to

$$EW = L_{1-10\ \rm keV}^{-0.52\pm0.27}(\rm erg/s) \times 10^{17.45\pm9.83}. \quad (2)$$

Baldwin (1977) observed an inverse correlation in the EW of CIV and the UV luminosity in AGNs. Analogously, the decrease in the EW of FeKα when increasing the X-ray luminosity is called the X-ray Baldwin effect. The dependence that we observe is compatible within the error with the one observed by Torrejón et al. (2010b) in X-ray binaries using a narrower energy range: $EW \propto L_{1.6-2.5\ \text{Å}}^{-0.29}$.

3.4.2. FeKα width vs. centroid energy

In Fig. 8 we present the centroid energy of this feature versus its width ($\sigma_{\rm line}$). We have successfully found a 90% confidence region of $\sigma_{\rm line}$ in 20 cases. We can see a moderate correlation (PC = 0.55), indicating a possible blending of lines. Two observations (uppermost side of Fig. 8) do not follow the correlation. They correspond to observations of 4U 1700-37 (Obs.ID 0083280201) and EXO 1722-363 (Obs.ID 0405640201) where the Fe complex is hardly resolved, and therefore it is very likely that a contribution of Fe XXV and Fe XXVI in the model of FeKα is increasing the measured width of the FeKα line.

Coloured squares correspond to the expected width from the contribution of three different broadening phenomena: line blending, Doppler shifts, and Compton broadening. A discussion of the different broadening contributions is given in Sect. 4.

3.4.3. Curve of growth

In Fig. 9 we show, for out-of-eclipse observations, the $N_{\rm H}$ versus the EW of FeKα (what is generally known as the curve of growth). We have successfully found a 90% confidence region of both $N_{\rm H}$ and EW in 46 cases. We want to take observations where $N_{\rm H}$ reflects the intrinsic absorption of the system into account, so we set $N_{\rm H} > 2$ as a condition to safely exceed the typical $N_{\rm H}$ of the interstellar medium for the sources here studied (checked using the online application following Willingale et al. 2013). The use of this criterion excludes the BeXB SAX J2103.5+4545, the γ Cassiopeae analogs: γ Cassiopeae and HD 110432; and the SFXT IGR J11215-5952. Moreover, eclipse observations show higher EW, and they are not comparable to out-of-eclipse observations. Therefore, eclipse observations have not been plotted in Fig. 9. As a consequence of the

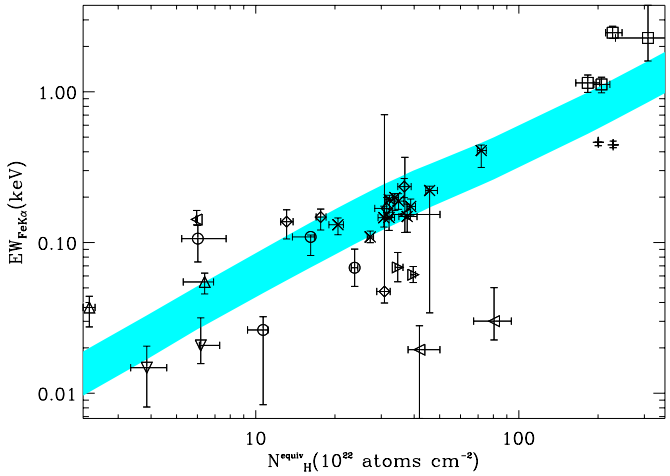

Fig. 9. Curve of growth observed for FeKα, that is, EW against $N_{\rm H}$. The turquoise band marks the expected correlation using numerical simulations. The sources are identified by different symbols when more than one observation is included: 4U 1700-37 (open circle), 4U 1907+09 (open upward triangle), Cygnus X-1 (open downward triangle), EXO1722-363 (open diamond), IGR J16318-4848 (open square), and IGR J16320-4751 (plus). Only one observation for Centaurus X-3, GX 301-2, Vela X-1, and XTE J0421+560 (all four a star symbol).

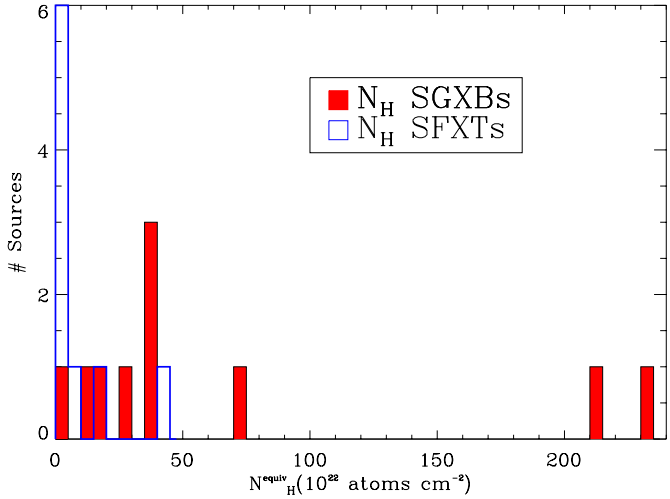

Fig. 10. Histograms showing a comparison of the $N_{\rm H}$ values observed in SGXBs (filled red) and SFXTs (empty blue).

chosen criteria, we end up with a set of 36 observations, where all the donors are supergiants.

Both $N_{\rm H}$ and the EW of FeKα are expected to correlate in HMXBs, as shown by Torrejón et al. (2010b), since the spectral lines are usually stronger when the optical depth increases. Our sample confirms these expectations, showing a notable correlation (PC = 0.85).

We have determined the theoretical curve of growth using numerical simulations. In this simulations there is an input of X-ray radiation with a power law profile, which is transmitted through a cloud of spherically distributed neutral matter (Eikmann 2012).

We took the power law index (Γ) in the simulations into account, since steeper profiles entail less photons available above the Fe K-shell threshold energy, thus decreasing the EW; that is to say, for the same $N_{\rm H}$, the higher Γ, the lower the EW of FeKα. In Fig. 9 the turquoise band traces the results from the simulations with $\Gamma \in [0.5, 2]$, which is the typical range where we find Γ in our fits.

3.5. $N_{\rm H}$: SGXBs and SFXTs

In Fig. 10 we have plotted histograms for the $N_{\rm H}$ values observed in SGXBs and SFXTs. Where we have more than one observation for the same source, we averaged the values to obtain one $N_{\rm H}$ that is representative of each system. The orbital phase critically affects the observed $N_{\rm H}$, and therefore ingress/egress and eclipse phases have not been taken into account.

We find that SGXBs are in general more absorbed than SFXTs. We performed a permutation test to quantify whether the observed disparity in the $N_{\rm H}$ is a random effect. We have ten $N_{\rm H}$ values for SGXBs and nine for SFXTs. We merged them in a set of 19 elements and considered every possible combination of two groups of ten and nine elements (92 378 possibilities). We compared the median of the two subsets and calculated the absolute difference: 99.7% of the cases have produced a lower absolute difference than the observed one. If using the mean instead of the median, the percentage is also very high (98.8%). In conclusion, it is very likely that the discrepancies in the observed $N_{\rm H}$ values for SGXBs and SFXTs are produced by physical reasons rather than arising by chance.

3.6. Individual sources analysis: IGR J16320-4751 and 4U 1700-37

3.6.1. IGR J16320-4751

IGR J16320-4751 was detected by *ASCA* in 1994 and 1997 (corresponding to AX J1631.9-4752), and by INTEGRAL in 2003 (Tomsick et al. 2003). It is a HMXB composed of an O8I optical star and a neutron star (Rahoui et al. 2008). It shows a modulation of 8.96 days, which is considered its orbital period (Corbet et al. 2005), and a pulsation period of ∼1300 s (Lutovinov et al. 2005). The ESA archives permitted eleven observations of IGR J16320-4751 to be collected, enabling us to study the curve of growth in more detail, as well as to track the absorption variation during the orbital phase.

In Fig. 11 we can see the curve of growth, as shown in Fig. 9, restricted to IGR J16320-4751. We clearly see the dependence between $N_{\rm H}$ and EW of FeKα, as stated for the bulk of the sources in Sect. 3.4.3, and the general trend following the numerical simulations. However, the agreement with the simulations is not completely fulfilled, given that the spectral fits of IGR J16320-4751 have led to a power law index $\Gamma \sim 0.5$ (see Table A.2). Since we expect more EW of FeKα from a lower power law index, the points for IGR J16320-4751 are expected to be located in the upper edge of the turquoise band, corresponding to the simulations with $\Gamma = 0.5$. We consider that the general trend is correct, but there are still some uncertainties in the fits and/or the theoretical hypothesis (spherical geometry and neutral matter).

From 14 August to 17 September 2008, there was a campaign of nine observations of IGR J16320-4751 by *XMM-Newton*. We used this set of data to plot the $N_{\rm H}$ modulation depending on the orbital phase (Fig. 12). We set $\phi = 0$ at the $N_{\rm H}$ maximum. We also calculated the theoretical absorption expected from a smooth wind in a non-eccentric orbit using a β velocity law (Castor et al. 1975) and the motion equation, considering the variations in the orbital inclination i, orbital separation

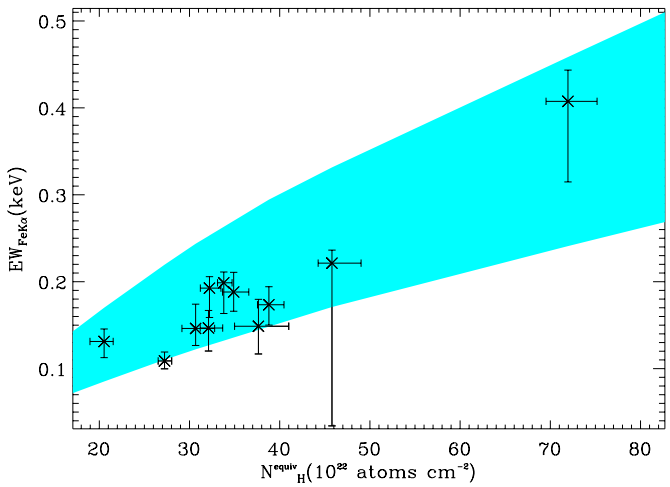

Fig. 11. EW of FeKα against $N_{\rm H}$, in IGR J16320-4751. The turquoise band marks the numerical simulations results, with $\Gamma \in [0.5, 2]$.

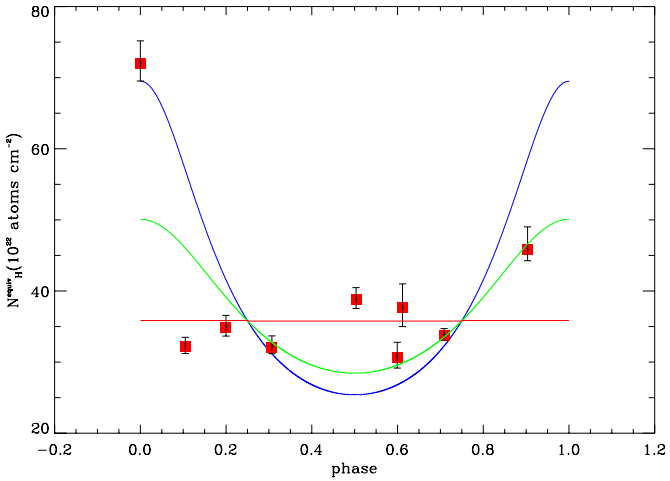

Fig. 12. Orbital modulation of $N_{\rm H}$ in the system IGR J16320-4751. Solid lines correspond to the expected absorption from a smooth wind and a non-eccentric orbit, assuming an orbital separation $a = 1.6\,R_\star$, $R_\star = 20\,R_\odot$, $\dot{M} = 10^{-5}\,M_\odot$/yr, $v_\infty = 700$ km s^{-1}, $\beta = 0.8$; and different orbital inclinations $i = 0, \pi/10, \pi/6$ rad (red, green, and blue).

a, star radius $R_\star$, mass loss rate $\dot{M}$, parameter β, and the terminal velocity of the wind v_∞.

Indeed, $\dot{M}$ and v_∞ cannot be distinguished in this simple model, so the actual parameter used is $\dot{M}/v_\infty$. However, hereafter we give values of $\dot{M}$ and v_∞ as if they were free variables, since they are much more commonly used than $\dot{M}/v_\infty$ in the literature. This way, we constrain our parameters to the observed and predicted range of values in O supergiants: $\dot{M} = 10^{-7}$–$10^{-5}\,M_\odot$/yr and $v_\infty = 500$–3000 km s^{-1} (Kudritzki & Puls 2000; Vink et al. 2001).

For a null orbital inclination, we obviously obtain a flat $N_{\rm H}$ modulation (Fig. 12), which describes the observed $N_{\rm H}$ (except at $\phi = 0$), assuming $a = 1.6\,R_\star$, $R_\star = 20\,R_\odot$, $\dot{M} = 10^{-5}\,M_\odot$/yr, $v_\infty = 700$ km s^{-1}, and $\beta = 0.8$. Gradually increasing the orbital inclination ($i = \pi/10, \pi/6$ rad), we are able to describe a high $N_{\rm H}$ at $\phi = 0$, but losing similarities around other orbital phases. Given the simplicity of the model, the obtained parameters are certainly just indicative.

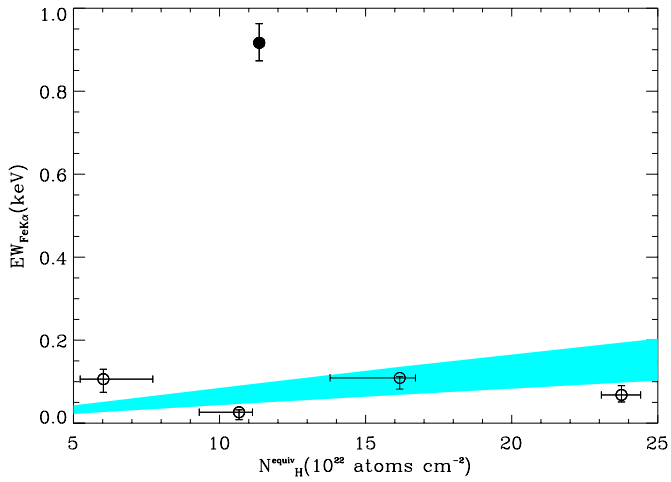

Fig. 13. EW of FeKα against $N_{\rm H}$, in 4U 1700-37. The filled circle corresponds to an eclipse observation. The turquoise band traces the numerical calculations with $\Gamma \in [0.5, 2]$.

3.6.2. 4U 1700-37

The source 4U 1700-37 was detected for the first time by *Uhuru* in 1970 (Jones et al. 1973). The optical star is HD 153919, an O6.5Iaf located at a distance of 1.9 kpc (Ankay et al. 2001). The orbital period is 3.41 days. Since X-ray pulsations have not been detected so far, the compact object can either be a neutron star or a black hole. The database of ESA contains five observations of 4U 1700-37, which we split into nine spectra to distinguish different states of the source.

In Fig. 13 we can see the curve of growth for 4U 1700-37. Although seven of the nine spectra show FeKα, we were able to constrain the boundaries of $N_{\rm H}$ in only five of the analyses. One of them corresponds to an eclipse observation. It shows much more EW because the continuum flux is blocked by the optical star, whereas FeKα comes from a more extended region that is not completely hidden during eclipse. We do not see any obvious dependence between $N_{\rm H}$ and EW, although the points lie in a region close to the expected values (turquoise band). Either way, a set of four observations (excluding the eclipse) is too small to perform a statistical analysis.

From 17 to 20 February 2001, 4U 1700-37 was observed by *XMM-Newton* four times in a campaign covering different orbital phases. We can therefore study the orbital modulation of $N_{\rm H}$ in the same way as we did with IGR J16320-4751, but including more constraints coming from the non-LTE analysis of Clark et al. (2002), where the following parameters are derived: $R_\star = 21.9\,R_\odot$, $\dot{M} = 9.5 \times 10^{-6}\,M_\odot$/yr, $v_\infty = 1750$ km s^{-1}, and $\beta = 1.3$. Considering that it is an eclipsing binary, we assume $i \sim \pi/2$. Therefore the only free parameter in our toy model is the orbital separation a. The best agreement is achieved when $a = 1.4\,R_\star$ (see Fig. 14). This orbital separation is consistent (in absolute units) with previous estimations of Conti & Cowley (1975) ($R_\star = 20\,R_\odot$, $a = 1.35\,R_\star$) and Heap & Corcoran (1992) ($R_\star = 18 \pm 3\,R_\odot$, $a = 2.0 \pm 0.4\,R_\star$).

4. Discussion

In Fig. 5 we have shown the centroid energies of FeKα. The distribution of the histogram is roughly Gaussian with a standard deviation that reflects the uncertainties in the fits. However, four values are too high to be compatible with this distribution, and all of them belong to Cygnus X-1. It can be caused either by

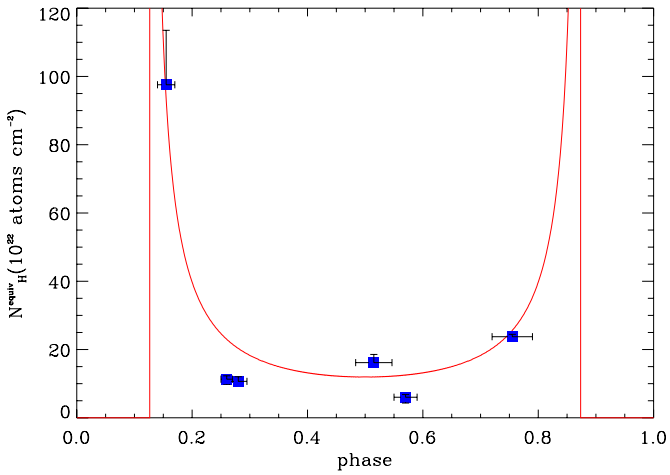

Fig. 14. Orbital modulation of $N_{\rm H}$ in 4U 1700-37. The solid line corresponds to the expected absorption from a smooth wind and a non-eccentric orbit, assuming the stellar values obtained in Clark et al. (2002), an orbital inclination $i \sim \pi/2$ rad, and an orbital separation $a = 1.4\,R_\star$.

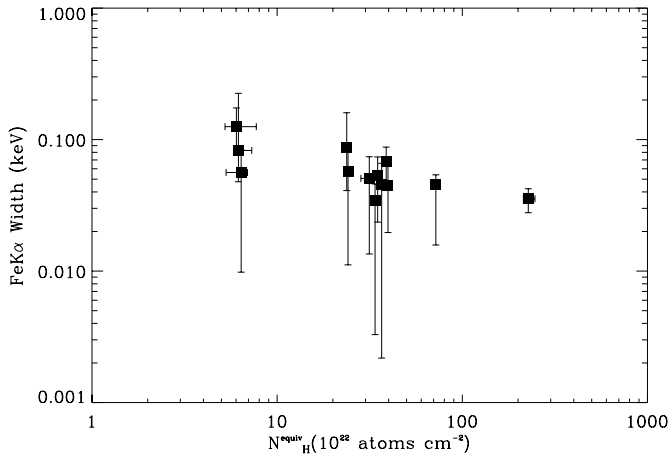

Fig. 15. Total equivalent hydrogen column ($N_{\rm H}$) against the width of FeKα.

an inadequate fit or for a physical reason. As stated before, in Cygnus X-1 we detect a broad Fe feature, interpreted as a relativistically broadened fluorescence line. However, we modelled the relativistically broadened feature with a Gaussian profile, which gives an acceptable fit, but might be inadequate, thereby affecting the parameters of the narrow FeKα arising from the fits. Alternatively, as a plausible physical explanation, in Cygnus X-1 the matter is accreted via an accretion disk, in contrast to the wind-fed accretion of most of the sources showing FeKα in this study. Therefore, the physical properties of the region emitting fluorescence might be different in Cygnus X-1 and the rest of systems. If this region is hotter in Cygnus X-1, the centroid energy of FeKα would be shifted to higher energies, as we observe.

IGR J16318-4848 is one of the most absorbed systems in the sample, and it presents a special configuration of matter in its surroundings where dust and cold gas distribute in a non-spherical manner, forming a disk-like structure of matter up to ~100 $R_\star$ (Chaty & Rahoui 2012). A likely high inclination of the system would produce the extreme X-ray absorption and the eclipse-like correlation between FeKα and continuum fluxes.

In Fig. 8 we see that the centroid energy of FeKα is higher when the line is broader. When more ionized Fe goes along with more variety in the Fe ions involved in the total emission, the width resulting from the blending of lines must depend on the centroid energy of the line, as observed. We have estimated the broadening produced in the lines by line blending by $\sigma_{\rm B} \approx E - 6.4$ (keV), with E the centroid energy of the line in keV. We note that it is also plausible that unresolved Fe XXV and Fe XXVI actually shift and broaden FeKα, producing an equivalent effect.

More processes are also able to significantly broaden FeKα. We have considered Compton broadening and Doppler shifts as plausible candidates. Compton scattering has been proposed as a possible broadening mechanism of emission lines in neutron star LMXBs (Díaz Trigo et al. 2012, for GX 13+1). For HMXBs, Compton broadening might also be significant, given the high $N_{\rm H}$ values observed (and the consequent high number of free electrons). However, if this process is what determines the width of the lines, we should observe a direct correlation between the absorption column and the line width. In Fig. 15 we can see that such a direct correlation is not present. Moreover, an inverse correlation is plausible. Cackett & Miller (2013) have analysed three neutron-star LMXBs and arrived at a similar result. Therefore, Compton broadening cannot be considered as mainly responsible for the observed width in HMXBs, although it is not ruled out as a modest contributor. We assign $\sigma_{\rm C}$ to the contribution of Compton scattering in the line broadening.

To estimate $\sigma_{\rm C}$, we used an empirical formula accurate to within 30%, derived from Kallman (1989) and corrected in Brandt & Matt (1994):

$$\sigma_{\rm C} = 0.019\,E_K\,\tau_{\rm Th}\,(1 + 0.78kT_{\rm e}) \simeq 0.12\,\tau_{\rm Th}\,(1 + 0.78kT_{\rm e})$$

where $E_K \simeq 6.4$ keV is the energy of FeKα, $\tau_{\rm Th}$ is the Thomson optical depth, and $kT_{\rm e}$ the electronic temperature in keV. We use $\tau_{\rm Th} = \sigma_{\rm Th} \int n_{\rm e}(s)\,{\rm d}s = \sigma_{\rm Th}\,N_{\rm e}$, where $\sigma_{\rm Th}$ is the Thomson cross section, $n_{\rm e}$ the electron number density, and where the integral is calculated along the line of sight. Assuming solar abundances, a temperature $kT_{\rm e} \ll 1$ keV and an almost completely ionized matter, as reasonable for galactic massive stars atmospheres, we obtain (see e.g. Eq. (3.61) in Novotny 1973):

$$N_{\rm e} = \int \frac{\rho(s)\,{\rm d}s}{2m_{\rm H}}(1+X) = \frac{X\,(1+X)}{2}\,N_{\rm H} \approx 0.7\,N_{\rm H}$$
$$\Rightarrow\ \sigma_{\rm C} \approx 0.5\,N_{\rm H}\left(10^{22}\,{\rm cm}^2\right)\ {\rm eV}.$$

Doppler shifts must be taken into account, since a velocity of more than 500 km s^{-1} (a very feasible speed, either in the wind or in the accretion flow) would broaden the lines by more than 10 eV. We assign $\sigma_{\rm D}$ to any broadening produced by Doppler effects.

Line blending, Compton scattering, and Doppler shifts produce a resultant width of

$$\sigma_{\rm total} = \sqrt{\sigma_{\rm B}^2 + \sigma_{\rm C}^2 + \sigma_{\rm D}^2}.$$

We adopted $\sigma_{\rm D} = 20, 40$ (eV) corresponding to velocities of $V \approx 1000, 2000$ km s^{-1}, which are very plausible either in the wind of the supergiant or in the accretion flow. We overplotted the corresponding values of $\sigma_{\rm total}$ in Fig. 8. For each observation, we computed the expected value ($\sigma_{\rm D} = 20$ (eV) and $\sigma_{\rm D} = 40$ (eV)). The vast majority of the line widths can be described in this way.

In IGR J16318-4848, the high absorption measured (above 2×10^{24} cm^2) and the consequent expected Compton broadening of more than 100 eV are not congruent with the measured width of ~35 eV. This is another indication that the absorbing matter in this system is cold and not ionized, as already

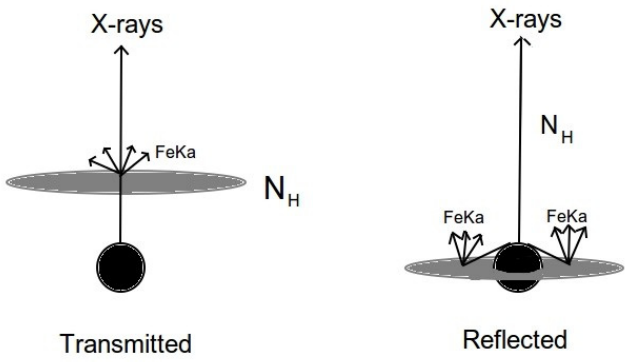

Fig. 16. Simple sketch of two plausible configurations of circumstellar matter in HMXBs. On the left side, X-rays are transmitted through a dense medium (e.g. the strong wind of the donor), producing high $N_{\rm H}$ directly correlated with the EW of FeKα. On the right side, X-rays are reflected in an accretion disk producing fluorescence and also transmitted through a more diffuse medium. In this case $N_{\rm H}$ is not necessarily correlated with the EW of FeKα.

stated by Chaty & Rahoui (2012). The employed expression for describing $\sigma_{\rm c}$ therefore cannot apply here, since there are not enough free electrons to broaden the line by means of Compton scattering.

In Fig. 9, we show the curve of growth of FeKα. We require that $N_{\rm H} > 2$ (intrinsic absorption rather than interstellar). In our sample, this criterion constrains the systems in Fig. 9 to those with supergiant donors alone. We observe a direct correlation between $N_{\rm H}$ and the EW. This correlation highlights that the X-ray absorption is strongly linked to the matter that emits FeKα, since it is produced by matter in the line of sight, where the X-rays are absorbed, and not in other plausible regions such as an accretion disk. (see a sketch in Fig. 16). In the systems included in Fig. 9 (all with a supergiant optical star), FeKα is produced from the transmission of X-rays through the circumstellar medium, that is, either through the strong wind of the supergiant donor or through any structure in the line of sight, such as ionization or accretion wakes. The hypothetical reflection of X-rays in an independent medium might produce an additional amount of FeKα, as observed in the BeXB GRO J1008−57 by Kühnel et al. (2013), which is not noticeable in the systems shown in Fig. 9.

As stated before, the region where fluorescence is emitted must be more extended than $R > R_{\star}$, and consequently the wind of the companion star, which is illuminated by the X-ray source, is an obvious contributor to both the absorption and the FeKα emission. The orbital modulation of $N_{\rm H}$ shown in Figs. 12 and 14 also support this interpretation.

Moreover, most of the observations track the numerical simulations assuming a characteristic range of Γ values, indicating that an isotropic distribution of absorbing (and FeKα emitting) matter is not far from reality. We do not ignore the variability and heterogeneous properties of the HMXBs environment, that might be reflected in the observed dispersion of the curve of growth and in the moderate discrepancies regarding the simplified view of spherically distributed neutral matter.

In Fig. 10 we have compared the observed values of $N_{\rm H}$ for SGXBs and SFXTs. We observed that SGXBs are in general more absorbed sources than SFXTs. This implies that, in SGXBs, either the compact object orbits a denser region of the donor wind, or else the interaction compact object – wind modifies the environment, producing an enhancement of density in its surroundings.

We took a look at the orbital parameters of SFXTs (see e.g. Table 2 in Romano et al. 2014) and find that their orbital periods lie in a wide range of values, from around three days for IGR J16479-4514, up to 164 days for IGR J11215-5952. Some of them show high eccentricity. However, currently there is no complete description of the orbital parameters in SFXTs. Therefore, we cannot rule out the possibility that, in this sample, SFXTs are less absorbed than SGXBs because of the distance of the compact object to the donor star. In this regard, further studies of orbital parameters of SFXTs will be useful.

Regarding the interaction compact object – wind, hydrodynamic simulations show that the gravitational potential of the compact object, and the X-ray radiation field, can significantly modify the observed value of $N_{\rm H}$ (Manousakis & Walter 2011; Manousakis et al. 2012). In SGXBs, where the X-ray emission is more persistent, these effects might be stronger than in SFXTs, so notably increasing the absorption.

5. Conclusions

We performed the spectral analysis of the whole sample of publicly available EPN *XMM-Newton* observations of HMXBs until August 2013, in order to describe its FeKα emission. In total, the study involves 46 HMXBs, 21 of them showing significant FeKα emission. As expected, we dealt with a very heterogenous set of objects and states of the sources, which must be properly organized. We classified the systems in the following groups: BeXBs, SGXBs, SFXTs, γ Cass analogues, HMGBs, and peculiar sources. Furthermore, we divided the observations depending on the source behaviour in the following states: quiescence, flare, eclipse ingress/egress, and eclipse. With these criteria, we finally had a set of 108 spectra for our analysis, which led to the following conclusions:

- The spectral atlas gives a qualitative description of the different groups of HMXBs, especially recognizable for SGXBs (fluorescence but not recombination Fe lines), and γ Cass analogues (modelled by *mekal* models and presenting fluorescence and recombination Fe lines). FeKα is very likely a ubiquitous feature in HMXBs, but its detection strongly depends on the quality of the observations. SGXBs and SFXTs, which show the higher $N_{\rm H}$ among the HMXBs, tend to exhibit a more prominent Fe fluorescence.
- The value of the centroid energy of FeKα constrains the ionization state of the reprocessing material to be below Fe XVIII.
- The FeKα and continuum fluxes are well correlated, as expected for the fluorescence emission of matter illuminated from an X-ray source. The different coefficients of correlation for eclipse and out-of-eclipse observations agrees with previous eclipse observations of HMXBs, in the sense of showing that the FeKα is produced in a region that ranges from the vicinity of the X-ray source to distances that are close to or greater than the stellar radius.
- We confirm an inverse correlation between the X-ray luminosity and the EW of FeKα X-ray Baldwin effect. The γ Cass analogues do not follow this correlation. This suggests that the Fe Kα reprocessing scenario is fundamentally different in SGXBs and in γ Cass analogues.
- The width of FeKα is predominantly below 0.15 keV and can be widely explained by appealing to line blending, Compton broadening, and moderate Doppler shifts (~1000 km s^{-1}).
- The curve of growth in SGXBs shows a clear correlation between FeKα EW and $N_{\rm H}$, indicating a strong link between

the absorbing and the fluorescent matter. From numerical simulations, the assumption of spherically distributed absorbing matter is roughly correct for most of the SGXBs.
- The $N_{\rm H}$ values observed in SGXBs are higher than in SFXTs. The disparity is hardly produced by chance, as shown by a permutation test of the sample, denoting a fundamental physical reason beneath. Systematic differences in the orbital parameters or different interaction compact object – stellar wind are plausible candidates for explaining such a discrepancy.
- The orbital modulation of $N_{\rm H}$ in IGR J16320-4751 and 4U 1700-37, together with the aforementioned results, points to the stellar wind as the main contributor to both continuum absorption and FeKα emission in the case of supergiant donors.

In summary, we present the most comprehensive study of FeKα in HMXBs to date, complementing previous surveys at high resolution (Torrejón et al. 2010b). We have significantly increased the number of sources and extended the study to all major classes of massive binaries.

Acknowledgements. This work is based on observations obtained with *XMM-Newton*, an ESA science mission with instruments and contributions directly funded by ESA member states and the USA (NASA). This research made use of software obtained from NASA's High Energy Astrophysics Science Archive Research Center (HEASARC), a service of Goddard Space Flight Center and the Smithsonian Astrophysical Observatory. The work of A.G.G. has been supported by the Spanish MICINN under FPI Fellowship BES-2011-050874 associated to the project AYA2010-15431. Part of this research was possible thanks to a travel grant from the Deutscher Akademischer Austauschdienst. The authors acknowledge the help of the International Space Science Institute at Bern, Switzerland, and the Faculty of the European Space Astronomy Centre. This work was supported partially by the Generalitat Valenciana project number GV2014/088 and by the Vicerectorat d'Investigaci, Desenvolupament i Innovaci de la Universitat d'Alacant under grant GRE12-35. J.J.R.R. acknowledges the support by the Matsumae International Foundation fellowship No14G04. S.M.N. acknowledges the support of the Spanish Unemployment Agency for allowing her to continue her scientific collaborations during a critical situation in the Spanish research system.

References

Ankay, A., Kaper, L., de Bruijne, J. H. J., et al. 2001, A&A, 370, 170
Audley, M. D., Nagase, F., Mitsuda, K., Angelini, L., & Kelley, R. L. 2006, MNRAS, 367, 1147
Baldwin, J. A. 1977, ApJ, 214, 679
Bartlett, E. S., Coe, M. J., & Ho, W. C. G. 2013, MNRAS, 436, 2054
Baykal, A., Stark, M. J., & Swank, J. H. 2002, ApJ, 569, 903
Beardmore, A. P., Coe, M. J., Markwardt, C., et al. 2009, The Astronomer's Telegram, 1901, 1
Blay, P., Negueruela, I., Reig, P., et al. 2006, A&A, 446, 1095
Blondin, J. M., Kallman, T. R., Fryxell, B. A., & Taam, R. E. 1990, ApJ, 356, 591
Blondin, J. M., Stevens, I. R., & Kallman, T. R. 1991, ApJ, 371, 684
Bodaghee, A., Courvoisier, T. J.-L., Rodriguez, J., et al. 2007, A&A, 467, 585
Bozzo, E., Falanga, M., & Stella, L. 2008, ApJ, 683, 1031
Brandt, W. M., & Matt, G. 1994, MNRAS, 268, 1051
Cackett, E. M., & Miller, J. M. 2013, ApJ, 777, 47
Casares, J., Ribó, M., Ribas, I., et al. 2005, MNRAS, 364, 899
Cash, W. 1979, ApJ, 228, 939
Castor, J. I., Abbott, D. C., & Klein, R. I. 1975, ApJ, 195, 157
Chaty, S., & Rahoui, F. 2012, ApJ, 751, 150
Chaty, S., Rahoui, F., Foellmi, C., et al. 2008, A&A, 484, 783
Clark, J. S., Goodwin, S. P., Crowther, P. A., et al. 2002, A&A, 392, 909
Coe, M. J., Fabregat, J., Negueruela, I., Roche, P., & Steele, I. A. 1996, MNRAS, 281, 333
Coleiro, A., Chaty, S., Zurita Heras, J. A., Rahoui, F., & Tomsick, J. A. 2013, A&A, 560, A108
Conti, P. S., & Cowley, A. P. 1975, ApJ, 200, 133
Corbet, R., Barbier, L., Barthelmy, S., et al. 2005, The Astronomer's Telegram, 649, 1
Cox, N. L. J., Kaper, L., & Mokiem, M. R. 2005, A&A, 436, 661
Díaz Trigo, M., Sidoli, L., Boirin, L., & Parmar, A. N. 2012, A&A, 543, A50
Drave, S. P., Bird, A. J., Sidoli, L., et al. 2013, MNRAS, 433, 528
Dubus, G. 2013, A&ARv, 21, 64
Duro, R., Dauser, T., Wilms, J., et al. 2011, A&A, 533, L3
Eikmann, W. 2012, Master's thesis, Dr. Karl Remeis Observatory Bamberg, Astronomical Institute of the Friedrich-Alexander-University of Erlangen-Nïrnberg
Filliatre, P., & Chaty, S. 2004, ApJ, 616, 469
Fiocchi, M., Bazzano, A., Bird, A. J., et al. 2013, ApJ, 762, 19
Fürst, F., Suchy, S., Kreykenbohm, I., et al. 2011, A&A, 535, A9
González-Galán, A., Negueruela, I., Castro, N., et al. 2014, A&A, 566, A131
Gottwald, M., Parmar, A. N., Reynolds, A. P., et al. 1995, A&AS, 109, 9
Grimm, H.-J., Gilfanov, M., & Sunyaev, R. 2002, A&A, 391, 923
Hanke, M., Wilms, J., Nowak, M. A., et al. 2009, ApJ, 690, 330
Heap, S. R., & Corcoran, M. F. 1992, ApJ, 387, 340
Hutchings, J. B., Cowley, A. P., Crampton, D., van Paradijs, J., & White, N. E. 1979, ApJ, 229, 1079
Jones, C., Forman, W., Tananbaum, H., et al. 1973, ApJ, 181, L43
Kallman, T. R. 1989, in Two Topics in X-Ray Astronomy, Vol. 1: X Ray Binaries. Vol. 2: AGN and the X Ray Background, eds. J. Hunt, & B. Battrick, ESA SP, 296, 157
Kallman, T. R., Palmeri, P., Bautista, M. A., Mendoza, C., & Krolik, J. H. 2004, ApJS, 155, 675
Kaper, L., van der Meer, A., & Najarro, F. 2006, A&A, 457, 595
Karasev, D. I., Lutovinov, A. A., & Burenin, R. A. 2010, MNRAS, 409, L69
Kharchenko, N. V., Piskunov, A. E., Roeser, S., Schilbach, E., & Scholz, R.-D. 2005, VizieR Online Data Catalog: J/A+A/438/1163
Kinugasa, K., Torii, K., Hashimoto, Y., et al. 1998, ApJ, 495, 435
Kirsch, M. G. F., Schönherr, G., Kendziorra, E., et al. 2006, A&A, 453, 173
Kreykenbohm, I., Wilms, J., Kretschmar, P., et al. 2008, A&A, 492, 511
Kudritzki, R.-P., & Puls, J. 2000, ARA&A, 38, 613
Kühnel, M., Müller, S., Kreykenbohm, I., et al. 2013, A&A, 555, A95
Liu, Q. Z., van Paradijs, J., & van den Heuvel, E. P. J. 2006, A&A, 455, 1165
Lopes de Oliveira, R. 2007, Ph.D. Thesis, Instituto de Astronomia, Geofísica e Ciências Atmosféricas, Universidade de São Paulo, Brazil, Observatoire Astronomique, Université Louis Pasteur, France
Lopes de Oliveira, R., & Motch, C. 2011, ApJ, 731, L6
Lopes de Oliveira, R., Motch, C., Haberl, F., Negueruela, I., & Janot-Pacheco, E. 2006, A&A, 454, 265
Lopes de Oliveira, R., Smith, M. A., & Motch, C. 2010, A&A, 512, A22
Lucy, L. B., & White, R. L. 1980, ApJ, 241, 300
Lumb, D. H., Schartel, N., & Jansen, F. A. 2012, Opt. Eng., 51, 011009
Lutovinov, A., Rodriguez, J., Revnivtsev, M., & Shtykovskiy, P. 2005, A&A, 433, L41
Manousakis, A., & Walter, R. 2011, A&A, 526, A62
Manousakis, A., Walter, R., & Blondin, J. M. 2012, A&A, 547, A20
Martínez-Núñez, S., Torrejón, J. M., Kühnel, M., et al. 2014, A&A, 563, A70
Masetti, N., Pretorius, M. L., Palazzi, E., et al. 2006, A&A, 449, 1139
Mason, A. B., Clark, J. S., Norton, A. J., Negueruela, I., & Roche, P. 2009, A&A, 505, 281
Megier, A., Strobel, A., Galazutdinov, G. A., & Krełowski, J. 2009, A&A, 507, 833
Mewe, R., Gronenschild, E. H. B. M., & van den Oord, G. H. J. 1985, A&AS, 62, 197
Nagase, F. 1989, PASJ, 41, 1
Negueruela, I., & Reig, P. 2004, The Astronomer's Telegram, 285, 1
Negueruela, I., Roche, P., Fabregat, J., & Coe, M. J. 1999, MNRAS, 307, 695
Negueruela, I., Smith, D. M., Harrison, T. E., & Torrejón, J. M. 2006, ApJ, 638, 982
Nespoli, E., Fabregat, J., & Mennickent, R. 2007, The Astronomer's Telegram, 983, 1
Nespoli, E., Fabregat, J., & Mennickent, R. E. 2008, A&A, 486, 911
Ng, C., Díaz Trigo, M., Cadolle Bel, M., & Migliari, S. 2010, A&A, 522, A96
Novotny, E. 1973, Introduction to stellar atmospheres and interiors (New York: Oxford University Press)
Oskinova, L. M., Feldmeier, A., & Kretschmar, P. 2012, MNRAS, 421, 2820
Paizis, A., & Sidoli, L. 2014, MNRAS, 439, 3439
Pellizza, L. J., Chaty, S., & Negueruela, I. 2006, A&A, 455, 653
Rahoui, F., & Chaty, S. 2008, A&A, 492, 163
Rahoui, F., Chaty, S., Lagage, P.-O., & Pantin, E. 2008, A&A, 484, 801
Rakowski, C. E., Schulz, N. S., Wolk, S. J., & Testa, P. 2006, ApJ, 649, L111
Rauw, G., Nazé, Y., Spano, M., Morel, T., & Ud-Doula, A. 2013, A&A, 555, L9
Reig, P. 2011, Ap&SS, 332, 1
Reig, P., Negueruela, I., Fabregat, J., Chato, R., & Coe, M. J. 2005, A&A, 440, 1079
Reynolds, A. P., Bell, S. A., & Hilditch, R. W. 1992, MNRAS, 256, 631

Ribó, M., Negueruela, I., Blay, P., Torrejón, J. M., & Reig, P. 2006, A&A, 449, 687
Riquelme, M. S., Torrejón, J. M., & Negueruela, I. 2012, A&A, 539, A114
Rodes-Roca, J. J., Page, K. L., Torrejón, J. M., Osborne, J. P., & Bernabéu, G. 2011, A&A, 526, A64
Romano, P., La Parola, V., Vercellone, S., et al. 2011a, MNRAS, 410, 1825
Romano, P., Mangano, V., Cusumano, G., et al. 2011b, MNRAS, 412, L30
Romano, P., Krimm, H. A., Palmer, D. M., et al. 2014, A&A, 562, A2
Sadakane, K., Hirata, R., Jugaku, J., et al. 1985, ApJ, 288, 284
Sanford, P., Mason, K. O., & Ives, J. 1975, MNRAS, 173, 9
Serlemitsos, P. J., Boldt, E. A., Holt, S. S., Ramaty, R., & Brisken, A. F. 1973, ApJ, 184, L1
Sguera, V., Bazzano, A., Bird, A. J., et al. 2006, ApJ, 646, 452
Sguera, V., Bird, A. J., Dean, A. J., et al. 2007, A&A, 462, 695
Shakura, N., Postnov, K., Kochetkova, A., & Hjalmarsdotter, L. 2012, MNRAS, 420, 216
Shapiro, S. L., Lightman, A. P., & Eardley, D. M. 1976, ApJ, 204, 187
Shenavrin, V. I., Taranova, O. G., & Nadzhip, A. E. 2011, Astron. Rep., 55, 31
Sidoli, L., Romano, P., Ducci, L., et al. 2009, MNRAS, 397, 1528
Smith, D. M. 2004, The Astronomer's Telegram, 338, 1
Smith, M. A., & Balona, L. 2006, ApJ, 640, 491
Smith, D. M., Heindl, W. A., Markwardt, C. B., et al. 2006, ApJ, 638, 974
Steele, I. A., Negueruela, I., Coe, M. J., & Roche, P. 1998, MNRAS, 297, L5
Tjemkes, S. A., van Paradijs, J., & Zuiderwijk, E. J. 1986, A&A, 154, 77
Tomsick, J. A., Lingenfelter, R., Walter, R., et al. 2003, IAU Circ., 8076, 1
Torrejón, J. M., Negueruela, I., Smith, D. M., & Harrison, T. E. 2010a, A&A, 510, A61
Torrejón, J. M., Schulz, N. S., Nowak, M. A., & Kallman, T. R. 2010b, ApJ, 715, 947
van der Meer, A., Kaper, L., di Salvo, T., et al. 2005, A&A, 432, 999
Verner, D. A., Ferland, G. J., Korista, K. T., & Yakovlev, D. G. 1996, ApJ, 465, 487
Vink, J. S., de Koter, A., & Lamers, H. J. G. L. M. 2001, A&A, 369, 574
Walter, R., & Zurita Heras, J. 2007, A&A, 476, 335
Watanabe, S., Sako, M., Ishida, M., et al. 2006, ApJ, 651, 421
Willingale, R., Starling, R. L. C., Beardmore, A. P., Tanvir, N. R., & O'Brien, P. T. 2013, MNRAS, 431, 394
Wilms, J., Allen, A., & McCray, R. 2000, ApJ, 542, 914
Ziółkowski, J. 2005, MNRAS, 358, 851

Pages 15 to 31 are available in the electronic edition of the journal at http://www.aanda.org

Appendix A: Tables

Table A.1. Table of sources included in the sample of HMXBs.

Class	Source	Distance (kpc)	Reference (class)	Reference (distance)
BeXB	1A 0535+26	2.00 ± 0.70	Shenavrin et al. (2011)	Steele et al. (1998)
	2S 1845-024	10.00	Bodaghee et al. (2007)	Grimm et al. (2002)
	X Persei	0.80 ± 0.14	Liu et al. (2006)	Megier et al. (2009)
	AX J1820.5-1434	8.20 ± 3.50	Liu et al. (2006)	Kinugasa et al. (1998)
	RX J0146.9+6121	1.95	Liu et al. (2006)	Kharchenko et al. (2005)
	RX J0440.9+4431	3.30 ± 0.50	Liu et al. (2006)	Reig et al. (2005)
	RX J1037.5-5647	5.00	Liu et al. (2006)	Grimm et al. (2002)
	SAX J2103.5+4545	3.20 ± 0.80	Liu et al. (2006)	Baykal et al. (2002)
	Swift J045106.8-694803	50.60 ± 2.10	Beardmore et al. (2009)	Bartlett et al. (2013)
	V0332+53	7.50 ± 1.50	Liu et al. (2006)	Negueruela et al. (1999)
SGXB	4U 1538-522	6.40 ± 1.00	Liu et al. (2006)	Reynolds et al. (1992)
	4U 1700-37	2.12 ± 0.34	Liu et al. (2006)	Megier et al. (2009)
	4U 1907+09	5.00	Liu et al. (2006)	Cox et al. (2005)
	EXO1722-363	8.00 ± 2.50	Liu et al. (2006)	Mason et al. (2009)
	GX 301-2	3.04	Liu et al. (2006)	Kaper et al. (2006)
	IGR J16207-5129	6.10	Nespoli et al. (2008)	Nespoli et al. (2008)
	IGR J16318-4848	3.60 ± 2.60	Filliatre & Chaty (2004)	Filliatre & Chaty (2004)
	IGR J16320-4751	3.50	Coleiro et al. (2013)	Rahoui et al. (2008)
	IGR J16465-4507	12.50	Walter & Zurita Heras (2007)	Smith (2004)
	SAX J1802.7-2017	12.40	Torrejón et al. (2010a)	Torrejón et al. (2010a)
	Vela X-1	1.90 ± 0.20	Liu et al. (2006)	Sadakane et al. (1985)
	XTE J0421+560	5.00 ± 4.00	Liu et al. (2006)	–
SFXT	AXJ1841.0-0536	7.80 ± 0.74	Romano et al. (2011b)	Nespoli et al. (2007)
	IGR J00370+6122	3.00	González-Galán et al. (2014)	Negueruela & Reig (2004)
	IGR J11215-5952	6.20	Sguera et al. (2006)	Masetti et al. (2006)
	IGR J16328-4726	6.50 ± 3.50	Fiocchi et al. (2013)	Fiocchi et al. (2013)
	IGR J16418-4532	13.00	Sguera et al. (2006)	Drave et al. (2013)
	IGRJ16479-4514	7.50 ± 2.50	Romano et al. (2011a)	Chaty et al. (2008)
	XTE J1739-302	2.30 ± 0.60	Smith et al. (2006)	Negueruela et al. (2006)
	IGR J17544-2619	3.20 ± 1.00	Pellizza et al. (2006)	Pellizza et al. (2006)
	IGR J18450-0435	3.60	Sguera et al. (2007)	Coe et al. (1996)
	IGR J18483-0311	3.50 ± 0.50	Rahoui & Chaty (2008)	Rahoui & Chaty (2008)
γ-Cass-like	γ Cassiopeiae	0.12 ± 0.01	Lopes de Oliveira et al. (2010)	Megier et al. (2009)
	HD 110432	0.39 ± 0.05	Smith & Balona (2006)	Megier et al. (2009)
	HD 119682	1.11	Rakowski et al. (2006)	Kharchenko et al. (2005)
	HD 157832	0.53	Lopes de Oliveira & Motch (2011)	Lopes de Oliveira & Motch (2011)
	HD 161103	1.50 ± 0.50	Lopes de Oliveira et al. (2006)	Lopes de Oliveira et al. (2006)
	HD 45314	1.50 ± 0.26	Rauw et al. (2013)	Megier et al. (2009)
	SAO 49725	2.20 ± 0.60	Lopes de Oliveira et al. (2010)	Lopes de Oliveira et al. (2006)
	SS397	1.50 ± 0.20	Lopes de Oliveira (2007)	Riquelme et al. (2012)
HMGB	LS I +61 303	2.50	Dubus (2013)	Grimm et al. (2002)
	LS 5039	2.50 ± 0.10	Dubus (2013)	Casares et al. (2005)
O9.5V+NS	4U 2206+54	2.90 ± 0.20	Blay et al. (2006)	Riquelme et al. (2012)
disk-fed	Cen X-3	10.00 ± 1.00	Liu et al. (2006)	Hutchings et al. (1979)
BH-SGXB	Cygnus X-1	2.10 ± 0.25	Liu et al. (2006)	Ziółkowski (2005)
B1-2	AX J1749.1-2733	16.00 ± 3.50	Karasev et al. (2010)	Karasev et al. (2010)

Table A.2. Parameters of the continuum.

Source	Obs ID	State	Model	Gain	$\chi^2_{\rm Red}$	P_0	$L_{1-10\,\rm keV}$ (10^{33} erg/s)	$\sum N_{\rm H}$ (10^{22} cm^{-2})	Γ	kT_1 (keV)	kT_2 (keV)	kT_3 (keV)
1A 0535+26	0674180101	Q	TN_1	–	0.87	8.70E-01	$11.03^{+9.20}_{-6.39}$	$0.72^{+0.06}_{-0.07}$	$1.40^{+0.06}_{-0.08}$	$1.24^{+0.05}_{-0.06}$	–	–
2S 1845-024	0302970801	Q	T_5	–	0.73	7.67E-01	$15.93^{+2.54}_{-0.98}$	$8.82^{+2.80}_{-4.11}$	–	$4.72^{+10.76}_{-0.92}$	–	–
X Persei	0151380101	Q	T_{13}	–	1.34	3.68E-03	$72.42^{+27.82}_{-23.16}$	$0.50^{+0.04}_{-0.04}$	–	$1.67^{+0.05}_{-0.07}$	$10.87^{+5.49}_{-3.41}$	–
X Persei	0151380101	Q	TN_1	–	1.41	7.44E-04	$72.49^{+27.81}_{-23.17}$	$0.58^{+0.08}_{-0.06}$	$1.63^{+0.14}_{-0.11}$	$1.59^{+0.04}_{-0.04}$	–	–
X Persei	0600980101	Q	TN_1	–	1.28	1.06E-02	$86.94^{+33.07}_{-27.62}$	$0.39^{+0.09}_{-0.11}$	$1.34^{+0.13}_{-0.14}$	$1.08^{+0.12}_{-0.15}$	–	–
AX J1820.5-1434	0511010101	Q	T_5	–	0.53	9.92E-01	$12.05^{+14.36}_{-8.39}$	$7.85^{+2.64}_{-1.78}$	–	$2.05^{+0.29}_{-0.23}$	–	–
AX J1820.5-1434	0511010101	Q	N_1	–	0.60	9.77E-01	$12.37^{+14.36}_{-8.63}$	$14.21^{+3.60}_{-2.03}$	$1.34^{+0.35}_{-0.22}$	–	–	–
RX J0146.9+6121	0201160101	Q	TN_1	–	1.31	8.58E-03	$7.65^{+0.11}_{-0.12}$	0.90	$1.61^{+0.10}_{-0.08}$	$1.34^{+0.08}_{-0.09}$	–	–
RX J0440.9+4431	0653660101	Q	T_6	–	1.16	8.55E-02	$65.96^{+22.21}_{-18.86}$	$0.78^{+0.06}_{-0.07}$	–	$0.91^{+0.08}_{-0.06}$	$2.28^{+0.23}_{-0.12}$	–
RX J0440.9+4431	0653660101	Q	T_{10}	–	1.21	4.14E-02	$66.00^{+22.13}_{-18.91}$	$1.17^{+0.05}_{-0.05}$	–	$1.30^{+0.05}_{-0.05}$	$5.82^{+0.35}_{-0.35}$	–
RX J0440.9+4431	0653660101	Q	TN_1	–	1.24	2.54E-02	$66.06^{+22.26}_{-18.89}$	$1.22^{+0.12}_{-0.13}$	$0.95^{+0.12}_{-0.13}$	$1.38^{+0.09}_{-0.07}$	–	–
RX J1037.5-5647	0550560101	Q	T_9	–	1.02	4.16E-01	$11.58^{+0.33}_{-0.43}$	1.04	–	$4.42^{+0.37}_{-0.45}$	–	–
RX J1037.5-5647	0550560101	Q	TN_1	–	1.00	4.94E-01	$11.53^{+0.38}_{-0.38}$	1.04	$1.09^{+0.38}_{-0.12}$	$1.55^{+0.32}_{-0.22}$	–	–
SAX J2103.5+4545	0149550401	Q	T_{10}	–	1.26	1.77E-02	$805.54^{+459.66}_{-355.73}$	$0.79^{+0.06}_{-0.04}$	–	$2.46^{+0.06}_{-0.06}$	$1.53^{+0.08}_{-0.15}$	–
SAX J2103.5+4545	0149550401	Q	TN_1	–	1.24	2.69E-02	$806.39^{+462.07}_{-355.79}$	$0.83^{+0.11}_{-0.11}$	$0.96^{+0.24}_{-0.22}$	$2.15^{+0.12}_{-0.21}$	–	–
Swift J045106.8-694803	0679381401	Q	N_1	–	1.06	3.28E-01	$860.26^{+118.45}_{-112.25}$	$0.29^{+0.21}_{-0.15}$	$1.07^{+0.13}_{-0.10}$	–	–	–
V0332+53	0506190101	Q	T_5	–	0.60	7.58E-01	$0.19^{+0.14}_{-0.09}$	0.83	–	$0.40^{+0.08}_{-0.07}$	–	–
4U 1538-522	0152780201	EC	N_1	–	1.33	7.12E-03	$20.04^{+7.24}_{-6.07}$	$0.97^{+0.03}_{-0.03}$	$0.37^{+0.04}_{-0.05}$	–	–	–
4U 1538-522	0152780201	I/E	N_2	–	1.44	5.65E-04	$659.55^{+227.25}_{-192.86}$	$80.48^{+13.16}_{-13.17}$	$0.86^{+0.05}_{-0.05}$	–	–	–
4U 1700-37	0083280101	D	N_2	–	1.38	9.69E-03	$161.58^{+62.67}_{-52.25}$	$11.31^{+1.49}_{-0.99}$	$1.20^{+0.17}_{-0.11}$	–	–	–
4U 1700-37	0083280101	F	N_1	–	0.97	5.73E-01	$1790.09^{+645.31}_{-545.05}$	$10.67^{+0.46}_{-1.36}$	$1.10^{+0.07}_{-0.09}$	–	–	–
4U 1700-37	0083280101	Q	N_1	–	1.16	1.04E-01	$624.17^{+228.25}_{-190.74}$	15.49	1.22	–	–	–
4U 1700-37	0083280201	F	N_2	–	1.28	1.23E-02	$1952.17^{+693.31}_{-589.18}$	$16.17^{+0.54}_{-2.39}$	$1.12^{+0.10}_{-0.03}$	–	–	–
4U 1700-37	0083280201	Q	TN_2	–	0.90	7.98E-01	$619.13^{+224.34}_{-189.62}$	$6.02^{+1.69}_{-0.79}$	$1.35^{+0.54}_{-0.25}$	$2.59^{+0.14}_{-0.26}$	–	–
4U 1700-37	0083280201	Q	N_2	–	1.00	4.69E-01	$623.31^{+226.45}_{-190.77}$	$8.16^{+2.55}_{-0.72}$	$1.03^{+0.08}_{-0.04}$	–	–	–
4U 1700-37	0083280301	Q	N_2	–	1.14	1.20E-01	$718.06^{+259.67}_{-217.98}$	$23.76^{+0.65}_{-0.69}$	$1.00^{+0.04}_{-0.05}$	–	–	–
4U 1700-37	0083280401	EC	N_1	–	1.22	1.30E-01	$24.12^{+10.00}_{-8.93}$	11.66	0.51	–	–	–
4U 1700-37	0083280401	I/E	N_2	–	1.13	2.01E-01	$313.50^{+116.85}_{-99.84}$	97.57	0.58	–	–	–
4U 1700-37	0600950101	EC	N_1	–	1.18	6.97E-02	$16.64^{+5.93}_{-5.01}$	$11.36^{+0.15}_{-0.16}$	0.70	–	–	–
4U 1700-37	0600950101	EC	N_2	–	1.04	3.58E-01	$16.77^{+5.98}_{-5.05}$	$15.96^{+0.22}_{-0.20}$	0.70	–	–	–
4U 1907+09	0555410101	F	TN_1	–	1.10	1.89E-01	$1288.31^{+6.16}_{-4.92}$	$2.33^{+0.12}_{-0.12}$	$0.75^{+0.08}_{-0.09}$	$0.87^{+0.03}_{-0.04}$	–	–
4U 1907+09	0555410101	Q	TN_2	–	0.99	5.16E-01	$721.87^{+2.75}_{-3.28}$	$6.39^{+0.52}_{-1.09}$	$0.45^{+0.10}_{-0.10}$	$1.18^{+0.07}_{-0.03}$	–	–
4U 1907+09	0555410101	Q	N_2	–	1.13	1.30E-01	$718.59^{+3.08}_{-3.04}$	$9.10^{+1.03}_{-1.21}$	$1.14^{+0.02}_{-0.02}$	–	–	–
EXO1722-363	0206380401	Q	T_5	–	1.33	9.84E-03	$522.62^{+389.71}_{-279.02}$	$17.65^{+0.86}_{-0.68}$	–	$2.78^{+0.10}_{-0.09}$	–	–

Notes. Parameters of the continuum, including observation ID, state of the source, model (see Table 1), artificial gain (offset or slope), reduced χ^2, null hypothesis probability (P_0), luminosity between 1−10 keV ($L_{1-10\,\rm keV}$), total $N_{\rm H}$ (adding every absorption component), photon index (Γ), and temperature of thermal components (kT_i): *bbody*, *diskbb*, *bremss*, *mekal* or *cemekl* (depending on the model). Parameters frozen or unbounded are included without an error estimation. Therefore they are not used in the plots and the subsequent discussion. The possible states are: quiescence(Q), flare(F), eclipse ingress/egress(I/E), eclipse(E) and dip(D).

Table A.2. continued.

Source	Obs ID	State	Model	Gain	$\chi^2_{\rm Red}$	P_0	$L_{1-10\,\rm keV}$ (10^{33} erg/s)	$\sum N_{\rm H}$ (10^{22} cm^{-2})	Γ	kT_1 (keV)	kT_2 (keV)	kT_3 (keV)
EXO1722-363	0206380401	Q	N_1	–	1.28	2.30E-02	$528.75^{+393.88}_{-282.05}$	$24.14^{+1.41}_{-0.95}$	$0.78^{+0.09}_{-0.07}$	–	–	–
EXO1722-363	0405640201	EC	T_5	–	0.71	7.47E-01	$2.77^{+2.35}_{-1.61}$	$17.78^{+6.87}_{-3.72}$	–	4.94	–	–
EXO1722-363	0405640201	EC	N_1	–	0.85	5.79E-01	$2.82^{+2.59}_{-1.72}$	$19.87^{+21.04}_{-3.85}$	$-0.19^{+0.75}_{-0.28}$	–	–	–
EXO1722-363	0405640301	Q	T_5	–	0.91	7.42E-01	$474.87^{+357.48}_{-254.37}$	$13.10^{+0.77}_{-0.66}$	–	$2.71^{+0.11}_{-0.09}$	–	–
EXO1722-363	0405640301	Q	N_1	–	1.04	3.67E-01	$479.86^{+360.57}_{-257.24}$	$18.55^{+1.18}_{-0.88}$	$0.77^{+0.09}_{-0.08}$	–	–	–
EXO1722-363	0405640401	Q	T_5	–	1.09	2.69E-01	$181.41^{+136.89}_{-97.28}$	$36.68^{+2.28}_{-2.02}$	–	$3.14^{+0.21}_{-0.18}$	–	–
EXO1722-363	0405640401	Q	N_1	–	1.00	4.77E-01	$182.90^{+137.96}_{-98.01}$	$44.56^{+3.18}_{-2.00}$	$0.63^{+0.14}_{-0.09}$	–	–	–
EXO1722-363	0405640901	Q	N_1	–	1.14	1.50E-01	$203.03^{+150.31}_{-108.96}$	$30.84^{+1.59}_{-2.01}$	$0.97^{+0.18}_{-0.07}$	–	–	–
EXO1722-363	0405640801	Q	T_7	–	1.15	1.44E-01	$287.66^{+215.12}_{-153.67}$	$31.45^{+1.71}_{-3.11}$	–	$0.23^{+0.00}_{-0.07}$	$2.62^{+0.16}_{-0.09}$	–
GX 301-2	0555200401	F	N_3	slope	1.29	1.21E-02	$3412.87^{+5.83}_{-5.37}$	$200.37^{+0.53}_{-0.57}$	0.81	–	–	–
GX 301-2	0555200401	Q	N_3	slope	1.82	9.70E-09	$1334.78^{+3.30}_{-2.47}$	$228.22^{+0.49}_{-0.57}$	1.04	–	–	–
IGR J16207-5129	0402920201	Q	N_2	–	1.17	8.16E-02	$94.98^{+2.93}_{--0.63}$	16.27	1.27	–	–	–
IGR J16318-4848	0154750401	Q	T_5	–	1.12	2.31E-01	$11.11^{+22.83}_{-10.28}$	$227.17^{+19.61}_{-13.52}$	–	$2.89^{+0.43}_{-0.32}$	–	–
IGR J16318-4848	0154750401	Q	N_1	–	1.05	3.63E-01	$11.15^{+22.66}_{-10.31}$	$232.66^{+12.48}_{-8.47}$	$0.91^{+0.19}_{-0.17}$	–	–	–
IGR J16318-4848	0201000201	Q	T_5	–	0.89	7.12E-01	$11.56^{+23.87}_{-10.70}$	$206.14^{+15.62}_{-13.46}$	–	$2.67^{+0.39}_{-0.27}$	–	–
IGR J16318-4848	0201000201	Q	N_1	–	0.92	6.36E-01	$11.62^{+23.87}_{-10.75}$	$214.22^{+11.00}_{-9.48}$	$1.08^{+0.20}_{-0.16}$	–	–	–
IGR J16318-4848	0201000301	Q	T_5	–	0.73	6.83E-01	$3.61^{+8.26}_{-3.36}$	$309.57^{+49.52}_{-76.63}$	–	$2.15^{+2.90}_{-0.46}$	–	–
IGR J16318-4848	0201000301	Q	N_1	–	0.76	6.55E-01	$3.64^{+7.93}_{-3.39}$	$317.51^{+56.91}_{-14.71}$	$1.66^{+0.66}_{-0.11}$	–	–	–
IGR J16318-4848	0201000401	Q	T_5	–	1.12	2.57E-01	$7.52^{+15.62}_{-6.96}$	$182.75^{+20.34}_{-18.20}$	–	$2.55^{+0.45}_{-0.31}$	–	–
IGR J16318-4848	0201000401	Q	N_1	–	1.16	2.12E-01	$7.56^{+15.54}_{-7.00}$	$191.92^{+21.91}_{-8.77}$	$1.19^{+0.45}_{-0.20}$	–	–	–
IGR J16320-4751	0128531101	Q	T_5	–	0.99	4.94E-01	$78.37^{+69.98}_{-45.61}$	$24.97^{+5.10}_{-4.87}$	–	$2.19^{+0.33}_{-0.23}$	–	–
IGR J16320-4751	0128531101	Q	T_{11}	–	1.03	4.23E-01	$79.52^{+70.79}_{-45.66}$	$34.91^{+1.50}_{-4.88}$	–	50.75	–	–
IGR J16320-4751	0128531101	Q	N_1	–	1.03	4.16E-01	$79.73^{+69.23}_{-46.82}$	$35.37^{+8.66}_{-4.55}$	$1.41^{+0.45}_{-0.28}$	–	–	–
IGR J16320-4751	0201700301	F	N_2	–	0.89	8.13E-01	$918.65^{+724.71}_{-515.23}$	$20.53^{+1.00}_{-1.57}$	$0.45^{+0.12}_{-0.13}$	–	–	–
IGR J16320-4751	0201700301	Q	N_2	–	0.93	6.96E-01	$417.44^{+328.31}_{-233.15}$	$27.23^{+0.80}_{-0.70}$	$0.65^{+0.07}_{-0.05}$	–	–	–
IGR J16320-4751	0556140101	Q	N_2	–	0.99	5.15E-01	$474.86^{+382.82}_{-267.46}$	$45.79^{+3.23}_{-1.53}$	$0.73^{+0.13}_{-0.08}$	–	–	–
IGR J16320-4751	0556140201	Q	N_2	–	1.05	3.47E-01	$920.37^{+729.24}_{-515.52}$	$32.21^{+1.27}_{-1.01}$	$0.39^{+0.07}_{-0.06}$	–	–	–
IGR J16320-4751	0556140301	Q	N_2	–	1.09	2.28E-01	$890.63^{+705.54}_{-498.80}$	$32.11^{+1.58}_{-0.92}$	$0.43^{+0.09}_{-0.05}$	–	–	–
IGR J16320-4751	0556140401	Q	N_2	–	1.21	6.25E-02	$547.92^{+436.81}_{-307.19}$	$38.80^{+1.67}_{-1.26}$	$0.72^{+0.08}_{-0.07}$	–	–	–
IGR J16320-4751	0556140501	Q	N_2	–	0.84	8.57E-01	$443.72^{+363.15}_{-251.54}$	$37.64^{+3.36}_{-2.65}$	$0.67^{+0.17}_{-0.12}$	–	–	–
IGR J16320-4751	0556140601	Q	N_2	–	1.04	3.73E-01	$1145.80^{+902.57}_{-640.15}$	$33.80^{+0.92}_{-0.69}$	$0.32^{+0.05}_{-0.03}$	–	–	–
IGR J16320-4751	0556140701	Q	N_2	–	1.24	5.34E-02	$418.19^{+333.69}_{-234.89}$	$71.96^{+3.22}_{-2.43}$	$0.17^{+0.08}_{-0.07}$	–	–	–
IGR J16320-4751	0556140801	Q	N_2	–	1.15	1.31E-01	$533.78^{+425.72}_{-299.24}$	$34.90^{+1.67}_{-1.24}$	$0.53^{+0.09}_{-0.06}$	–	–	–
IGR J16320-4751	0556141001	Q	N_2	–	0.93	7.05E-01	$666.20^{+530.68}_{-373.27}$	$30.68^{+2.11}_{-1.52}$	$0.52^{+0.12}_{-0.08}$	–	–	–
IGR J16465-4507	0164561001	Q	N_1	–	0.58	9.23E-01	$74.04^{+6.11}_{-8.28}$	$72.18^{+24.40}_{-15.83}$	$0.42^{+0.55}_{-0.50}$	–	–	–
SAX J1802.7-2017	0206380601	Q	N_1	–	1.28	3.18E-02	$624.71^{+16.86}_{-20.14}$	$15.72^{+1.99}_{-1.35}$	$0.96^{+0.19}_{-0.13}$	–	–	–
Vela X-1	0111030101	F	N_2	–	1.35	4.24E-03	$547.45^{+126.06}_{-112.92}$	$34.63^{+1.64}_{-0.77}$	$1.66^{+0.13}_{-0.07}$	–	–	–
Vela X-1	0111030101	Q	N_1	–	0.87	8.65E-01	$323.43^{+73.19}_{-65.56}$	$39.68^{+0.82}_{-0.82}$	$1.65^{+0.05}_{-0.06}$	–	–	–
XTE J0421+560	0139760101	Q	N_1	–	0.70	9.51E-01	$3.99^{+9.48}_{-3.84}$	$36.88^{+13.28}_{-3.76}$	$0.57^{+0.44}_{-0.26}$	–	–	–

Table A.2. continued.

Source	Obs ID	State	Model	Gain	$\chi^2_{\rm Red}$	P_0	$L_{1-10\,\rm keV}$ (10^{33} erg/s)	$\sum N_{\rm H}$ (10^{22} cm^{-2})	Γ	kT_1 (keV)	kT_2 (keV)	kT_3 (keV)
AXJ1841.0-0536	0604820301	F	N_3	–	1.39	1.54E-03	$501.72^{+104.41}_{-94.20}$	$41.90^{+8.22}_{-3.98}$	$1.27^{+0.07}_{-0.05}$	–	–	–
IGR J00370+6122	0501450101	Q	T_{10}	–	0.84	9.23E-01	$47.94^{+0.64}_{-0.60}$	$0.87^{+0.13}_{-0.09}$	–	$1.16^{+0.09}_{-0.08}$	$4.20^{+0.69}_{-0.55}$	–
IGR J00370+6122	0501450101	Q	T_6	–	0.91	7.71E-01	$47.70^{+0.75}_{-0.62}$	0.65	–	$0.76^{+0.07}_{-0.05}$	$1.89^{+0.18}_{-0.10}$	–
IGR J00370+6122	0501450101	Q	T_9	–	0.97	5.92E-01	$47.95^{+0.59}_{-0.68}$	$1.17^{+0.05}_{-0.05}$	–	$3.08^{+0.09}_{-0.09}$	–	–
IGR J00370+6122	0501450101	Q	TN_1	–	0.84	9.24E-01	$48.01^{+0.58}_{-0.74}$	$1.00^{+0.17}_{-0.13}$	$1.16^{+0.19}_{-0.14}$	$1.28^{+0.11}_{-0.07}$	–	–
IGR J11215-5952	0405181901	F	TN_1	–	1.04	3.64E-01	$639.50^{+5.64}_{-5.72}$	$0.89^{+0.09}_{-0.06}$	$1.04^{+0.15}_{-0.09}$	$1.87^{+0.26}_{-0.23}$	–	–
IGR J11215-5952	0405181901	Q	TN_1	–	0.98	5.39E-01	$76.78^{+0.87}_{-0.97}$	$1.02^{+0.21}_{-0.12}$	$0.63^{+0.21}_{-0.15}$	$1.22^{+0.14}_{-0.06}$	–	–
IGR J16328-4726	0654190201	Q	T_5	–	1.04	3.77E-01	$32.07^{+45.82}_{-25.42}$	$16.67^{+1.32}_{-1.25}$	–	$2.14^{+0.11}_{-0.10}$	–	–
IGR J16328-4726	0654190201	Q	T_9	–	1.03	3.93E-01	$32.35^{+46.00}_{-25.65}$	$22.21^{+1.58}_{-0.95}$	–	$4.48^{+0.45}_{-0.59}$	–	–
IGR J16328-4726	0654190201	Q	N_1	–	1.07	2.98E-01	$32.54^{+46.43}_{-25.80}$	$25.13^{+2.26}_{-1.62}$	$1.41^{+0.18}_{-0.13}$	–	–	–
IGR J16418-4532	0206380301	Q	T_5	–	0.90	7.30E-01	$122.35^{+4.58}_{-4.50}$	$10.73^{+1.42}_{-1.18}$	–	$2.11^{+0.15}_{-0.13}$	–	–
IGR J16418-4532	0206380301	Q	N_1	–	0.91	7.01E-01	$124.60^{+4.33}_{-5.00}$	$17.64^{+2.35}_{-1.53}$	$1.35^{+0.22}_{-0.15}$	–	–	–
IGR J16418-4532	0405180501	Q	T_5	–	1.11	1.99E-01	$78.92^{+2.30}_{-2.38}$	$3.92^{+0.42}_{-0.36}$	–	$1.77^{+0.07}_{-0.07}$	–	–
IGR J16418-4532	0405180501	Q	N_1	–	1.10	2.26E-01	$82.17^{+2.23}_{-2.32}$	$8.25^{+0.77}_{-0.57}$	$1.49^{+0.12}_{-0.10}$	–	–	–
IGRJ16479-4514	0512180101	EC	N_1	–	0.95	5.92E-01	$5.30^{+4.63}_{-3.10}$	$8.21^{+1.62}_{-1.14}$	$1.75^{+0.32}_{-0.26}$	–	–	–
IGRJ16479-4514	0512180101	I/E	N_3	–	0.74	9.67E-01	$278.33^{+225.37}_{-159.69}$	69.51	1.12	–	–	–
XTE J1739-302	0554720101	F	T_5	–	1.25	5.66E-02	$1.61^{+1.05}_{-0.76}$	$1.51^{+0.21}_{-0.18}$	–	$1.37^{+0.05}_{-0.05}$	–	–
XTE J1739-302	0554720101	F	T_{11}	–	1.08	2.88E-01	$1.71^{+1.11}_{-0.80}$	$3.81^{+0.31}_{-0.32}$	–	$10.46^{+3.51}_{-1.84}$	–	–
XTE J1739-302	0554720101	F	N_1	–	1.20	9.43E-02	$1.73^{+1.11}_{-0.82}$	$4.29^{+0.46}_{-0.33}$	$1.81^{+0.13}_{-0.10}$	–	–	–
XTE J1739-302	0554720101	Q	T_5	–	1.20	2.51E-01	$0.16^{+0.12}_{-0.08}$	$1.89^{+1.12}_{-0.81}$	–	$1.00^{+0.13}_{-0.12}$	–	–
XTE J1739-302	0554720101	Q	T_{11}	–	1.39	1.26E-01	$0.17^{+0.13}_{-0.09}$	$4.15^{+1.50}_{-1.08}$	–	$3.92^{+2.55}_{-1.37}$	–	–
XTE J1739-302	0554720101	Q	N_1	–	1.52	7.23E-02	$0.18^{+0.13}_{-0.09}$	$5.08^{+1.59}_{-0.92}$	$2.49^{+0.46}_{-0.30}$	–	–	–
XTE J1739-302	0561580101	F	T_5	–	0.96	6.04E-01	$5.68^{+3.63}_{-2.67}$	$2.24^{+0.26}_{-0.23}$	–	$1.67^{+0.06}_{-0.06}$	–	–
XTE J1739-302	0561580101	F	T_{11}	–	0.84	8.79E-01	$5.96^{+3.85}_{-2.79}$	$5.12^{+0.29}_{-0.42}$	–	$34.27^{+44.58}_{-8.96}$	–	–
XTE J1739-302	0561580101	F	N_1	–	0.88	8.05E-01	$6.00^{+3.81}_{-2.82}$	$5.31^{+0.50}_{-0.41}$	$1.43^{+0.11}_{-0.09}$	–	–	–
XTE J1739-302	0561580101	Q	T_5	–	1.24	6.93E-02	$1.14^{+0.74}_{-0.54}$	$2.28^{+0.29}_{-0.25}$	–	$1.42^{+0.06}_{-0.05}$	–	–
XTE J1739-302	0561580101	Q	T_{11}	–	1.02	4.33E-01	$1.20^{+0.79}_{-0.57}$	$4.94^{+0.38}_{-0.39}$	–	$10.85^{+3.85}_{-1.85}$	–	–
XTE J1739-302	0561580101	Q	N_1	–	1.09	2.77E-01	$1.22^{+0.78}_{-0.58}$	$5.52^{+0.63}_{-0.42}$	$1.82^{+0.15}_{-0.10}$	–	–	–
IGR J17544-2619	0148090501	F	T_5	–	0.90	7.16E-01	$16.58^{+13.39}_{-9.11}$	$2.10^{+0.34}_{-0.28}$	–	$1.32^{+0.07}_{-0.06}$	–	–
IGR J17544-2619	0148090501	F	T_{11}	–	0.81	8.91E-01	$17.77^{+14.39}_{-9.78}$	$4.58^{+0.40}_{-0.43}$	–	$8.60^{+3.08}_{-1.63}$	–	–
IGR J17544-2619	0148090501	F	N_1	–	0.87	7.83E-01	$18.12^{+14.45}_{-10.01}$	$5.17^{+0.75}_{-0.48}$	$1.92^{+0.21}_{-0.14}$	–	–	–
IGR J18450-0435	0306170401	F	TN_1	–	1.04	3.51E-01	$131.25^{+1.41}_{-1.55}$	$2.18^{+0.31}_{-0.24}$	$0.84^{+0.26}_{-0.22}$	$1.58^{+0.26}_{-0.13}$	–	–
IGR J18450-0435	0306170401	Q	TN_1	–	1.05	3.39E-01	$22.69^{+0.37}_{-0.46}$	$2.47^{+0.58}_{-0.27}$	$0.79^{+0.66}_{-0.19}$	$1.74^{+0.23}_{-0.08}$	–	–
IGR J18483-0311	0406140201	Q	T_5	–	1.17	1.98E-01	$1.25^{+0.48}_{-0.39}$	$4.64^{+1.11}_{-0.75}$	–	$1.36^{+0.09}_{-0.10}$	–	–
IGR J18483-0311	0406140201	Q	T_9	–	1.28	9.12E-02	$1.26^{+0.49}_{-0.39}$	$7.42^{+1.28}_{-0.83}$	–	$2.07^{+0.25}_{-0.22}$	–	–
IGR J18483-0311	0406140201	Q	N_1	–	1.39	4.16E-02	$1.29^{+0.48}_{-0.41}$	$11.40^{+0.53}_{-0.33}$	$2.44^{+0.15}_{-0.14}$	–	–	–
γ Cassiopeiae	0201220101	Q	T_3	slope	1.39	1.42E-03	$0.24^{+0.05}_{-0.05}$	0.56	–	0.96	5.27	33.04
γ Cassiopeiae	0651670201	Q	T_4	–	1.22	3.62E-02	$0.27^{+0.06}_{-0.05}$	$0.23^{+0.01}_{-0.02}$	–	$28.62^{+1.14}_{-0.92}$	–	–
γ Cassiopeiae	0651670201	Q	T_3	–	0.89	8.39E-01	$0.27^{+0.06}_{-0.05}$	$0.42^{+0.05}_{-0.04}$	–	0.74	3.42	31.13

Table A.2. continued.

Source	Obs ID	State	Model	Gain	$\chi^2_{\rm Red}$	P_0	$L_{1-10\,\rm keV}$ (10^{33} erg/s)	$\sum N_{\rm H}$ (10^{22} cm^{-2})	Γ	kT_1 (keV)	kT_2 (keV)	kT_3 (keV)
γ Cassiopeiae	0651670301	Q	T_3	–	1.43	4.40E-04	$0.24^{+0.05}_{-0.05}$	0.56	–	0.64	3.95	40.83
γ Cassiopeiae	0651670401	Q	T_3	offset	1.15	1.09E-01	$0.33^{+0.07}_{-0.07}$	0.56	–	0.66	3.58	38.62
γ Cassiopeiae	0651670501	Q	T_3	offset	1.18	6.73E-02	$0.23^{+0.05}_{-0.05}$	0.56	–	0.66	3.40	38.38
HD 110432	0504730101	Q	N_1	–	1.24	2.81E-02	$0.21^{+0.06}_{-0.06}$	$0.17^{+0.02}_{-0.02}$	$1.52^{+0.02}_{-0.02}$	–	–	–
HD 110432	0504730101	Q	TN_5	–	1.03	3.78E-01	$0.21^{+0.06}_{-0.06}$	$0.11^{+0.01}_{-0.02}$	$0.94^{+0.18}_{-0.15}$	$8.69^{+1.16}_{-1.14}$	–	–
HD 119682	0551000201	Q	T_2	–	1.11	2.06E-01	$0.16^{+0.01}_{-0.01}$	1.81	–	$0.22^{+0.00}_{-0.05}$	$14.53^{+9.04}_{-3.50}$	–
HD 119682	0551000201	Q	TN_3	–	1.18	1.06E-01	$0.16^{+0.01}_{-0.00}$	1.81	$1.63^{+0.15}_{-0.16}$	$0.12^{+0.00}_{-0.01}$	–	–
HD 157832	0551020101	Q	T_1	–	1.07	3.12E-01	$0.08^{+0.00}_{-0.00}$	0.34	–	$6.50^{+0.90}_{-0.73}$	–	–
HD 161103	0201200101	Q	T_2	–	1.20	9.76E-02	$0.41^{+0.34}_{-0.23}$	0.94	–	1.03	7.05	–
HD 45314	0670080301	Q	T_2	–	0.96	5.63E-01	$0.30^{+0.14}_{-0.10}$	0.73	–	1.03	13.29	–
SAO 49725	0201200201	Q	T_2	–	1.31	7.39E-02	$0.52^{+0.39}_{-0.27}$	0.77	–	0.82	$18.86^{+61.04}_{-2.80}$	–
SAO 49725	0201200201	Q	TN_5	–	1.19	1.67E-01	$0.55^{+0.41}_{-0.29}$	0.77	$0.82^{+0.40}_{-0.37}$	$1.97^{+0.92}_{-0.53}$	–	–
SS397	0122700101	Q	T_1	–	0.84	7.90E-01	$0.17^{+0.07}_{-0.05}$	1.37	–	$7.13^{+2.49}_{-1.14}$	–	–
SS397	0122700101	Q	N_1	–	1.00	4.67E-01	$0.17^{+0.06}_{-0.05}$	$1.45^{+0.43}_{-0.27}$	$1.73^{+0.24}_{-0.16}$	–	–	–
SS397	0122700201	Q	T_1	–	0.89	6.88E-01	$0.20^{+0.08}_{-0.06}$	1.37	–	$10.03^{+7.04}_{-2.09}$	–	–
SS397	0122700201	Q	N_1	–	0.93	6.04E-01	$0.20^{+0.08}_{-0.06}$	1.37	$1.58^{+0.12}_{-0.11}$	–	–	–
SS397	0122700301	Q	T_1	–	1.03	4.21E-01	$0.13^{+0.06}_{-0.04}$	1.37	–	$6.92^{+3.32}_{-1.23}$	–	–
SS397	0122700301	Q	N_1	–	1.08	3.35E-01	$0.14^{+0.06}_{-0.05}$	1.37	$1.68^{+0.13}_{-0.11}$	–	–	–
SS397	0122700501	Q	T_1	–	1.01	4.49E-01	$0.20^{+0.09}_{-0.06}$	1.37	–	$28.01^{+51.89}_{-11.74}$	–	–
SS397	0122700501	Q	N_1	–	0.95	5.45E-01	$0.19^{+0.09}_{-0.07}$	1.37	$1.42^{+0.20}_{-0.16}$	–	–	–
LS I +61 303	0207260101	Q	TN_1	–	1.09	2.25E-01	$6.27^{+0.08}_{-0.07}$	0.90	$1.98^{+0.05}_{-0.08}$	$2.46^{+1.65}_{-0.26}$	–	–
LS I +61 303	0505980801	Q	TN_1	–	1.03	4.04E-01	$5.89^{+0.13}_{-0.12}$	0.90	$2.34^{+0.12}_{-0.13}$	$1.78^{+0.33}_{-0.15}$	–	–
LS I +61 303	0505980901	Q	TN_1	–	1.19	8.86E-02	$6.31^{+0.20}_{-0.17}$	0.90	$2.47^{+0.17}_{-0.24}$	$1.85^{+0.34}_{-0.15}$	–	–
LS I +61 303	0505981001	Q	TN_1	–	1.09	2.44E-01	$6.00^{+0.18}_{-0.16}$	0.90	$2.28^{+0.16}_{-0.25}$	$1.79^{+0.57}_{-0.16}$	–	–
LS I +61 303	0505981101	Q	TN_1	–	0.92	7.24E-01	$6.39^{+0.16}_{-0.11}$	0.90	$2.08^{+0.09}_{-0.16}$	$2.17^{+2.48}_{-0.24}$	–	–
LS I +61 303	0505981201	Q	TN_1	–	0.99	5.09E-01	$11.94^{+0.24}_{-0.18}$	0.90	$1.89^{+0.07}_{-0.11}$	$2.58^{+1.74}_{-0.31}$	–	–
LS I +61 303	0505981301	Q	TN_1	–	1.06	3.03E-01	$9.37^{+0.18}_{-0.15}$	0.90	$2.07^{+0.11}_{-0.12}$	$2.07^{+0.34}_{-0.15}$	–	–
LS I +61 303	0505981401	Q	TN_1	–	1.16	1.03E-01	$6.22^{+0.17}_{-0.12}$	0.90	$2.06^{+0.11}_{-0.17}$	$2.12^{+1.23}_{-0.22}$	–	–
LS 5039	0151160201	Q	T_{11}	–	1.18	9.13E-02	$5.00^{+0.58}_{-0.52}$	1.03	–	$11.87^{+2.26}_{-1.18}$	–	–
LS 5039	0151160201	Q	N_1	–	0.97	5.76E-01	$5.10^{+0.56}_{-0.52}$	1.03	$1.60^{+0.04}_{-0.04}$	–	–	–
LS 5039	0151160301	Q	T_{11}	–	1.21	6.01E-02	$5.07^{+0.61}_{-0.53}$	1.03	–	$18.50^{+4.55}_{-2.57}$	–	–
LS 5039	0151160301	Q	T_{10}	–	1.20	6.97E-02	$5.08^{+0.64}_{-0.54}$	1.03	–	$2.01^{+0.42}_{-0.16}$	$0.76^{+0.16}_{-0.07}$	–
LS 5039	0151160301	Q	N_1	–	1.11	1.99E-01	$5.15^{+0.59}_{-0.55}$	1.03	$1.48^{+0.04}_{-0.04}$	–	–	–
LS 5039	0202950201	Q	T_{11}	–	1.15	1.14E-01	$5.93^{+0.62}_{-0.58}$	1.03	–	$14.66^{+1.68}_{-1.51}$	–	–
LS 5039	0202950201	Q	T_{10}	–	1.10	2.09E-01	$6.02^{+0.65}_{-0.62}$	1.03	–	$2.14^{+0.26}_{-0.16}$	$0.82^{+0.08}_{-0.06}$	–
LS 5039	0202950201	Q	N_1	–	0.93	6.99E-01	$6.05^{+0.63}_{-0.59}$	1.03	$1.54^{+0.03}_{-0.03}$	–	–	–
LS 5039	0202950301	Q	T_{11}	–	1.19	8.41E-02	$3.50^{+0.43}_{-0.38}$	1.03	–	$9.24^{+1.38}_{-0.93}$	–	–
LS 5039	0202950301	Q	N_1	–	0.92	7.12E-01	$3.60^{+0.41}_{-0.38}$	1.03	$1.69^{+0.04}_{-0.04}$	–	–	–
4U 2206+54	0650640101	Q	TN_1	–	1.19	5.04E-02	$294.46^{+42.83}_{-39.89}$	$0.61^{+0.03}_{-0.03}$	$1.01^{+0.04}_{-0.04}$	$1.67^{+0.04}_{-0.03}$	–	–

Table A.2. continued.

Source	Obs ID	State	Model	Gain	$\chi^2_{\rm Red}$	P_0	$L_{1-10\,\rm keV}$ (10^{33} erg/s)	$\sum N_{\rm H}$ (10^{22} cm^{-2})	Γ	kT_1 (keV)	kT_2 (keV)	kT_3 (keV)
Cen X-3	0111010101	I/E	TN_4	–	1.28	1.24E-02	$2242.27^{+477.52}_{-430.86}$	$5.96^{+0.04}_{-0.05}$	0.68	0.94	–	–
Cen X-3	0111010101	I/E	N_2	–	1.27	1.39E-02	$2240.60^{+477.65}_{-430.78}$	$6.07^{+0.08}_{-0.09}$	0.71	–	–	–
Cygnus X-1	0202401101	Q	TN_4	–	1.12	1.54E-01	$10191.40^{+2586.02}_{-2289.25}$	$3.85^{+0.74}_{-0.51}$	$2.67^{+0.06}_{-0.04}$	$0.46^{+0.01}_{-0.01}$	–	–
Cygnus X-1	0202401201	Q	TN_3	–	1.13	1.39E-01	$8572.45^{+2176.95}_{-1929.60}$	$0.77^{+0.02}_{-0.01}$	$2.61^{+0.05}_{-0.03}$	$0.43^{+0.00}_{-0.01}$	–	–
Cygnus X-1	0202760201	Q	N_1	–	1.49	2.94E-03	$5061.89^{+1284.05}_{-1137.75}$	0.86	$2.29^{+0.03}_{-0.01}$	–	–	–
Cygnus X-1	0202760301	Q	N_1	–	0.96	5.82E-01	$3453.30^{+877.54}_{-777.01}$	0.86	$2.07^{+0.01}_{-0.01}$	–	–	–
Cygnus X-1	0202760401	Q	N_1	–	1.72	6.18E-05	$5009.50^{+1269.64}_{-1126.79}$	0.86	$2.10^{+0.02}_{-0.01}$	–	–	–
Cygnus X-1	0202760501	Q	N_1	–	1.17	1.38E-01	$4842.41^{+1232.95}_{-1091.06}$	0.86	$2.18^{+0.02}_{-0.02}$	–	–	–
Cygnus X-1	0500880201	D	TN_4	–	1.19	6.15E-02	$1899.40^{+494.23}_{-430.07}$	$4.53^{+0.26}_{-0.34}$	$1.43^{+0.01}_{-0.03}$	$0.39^{+0.02}_{-0.02}$	–	–
Cygnus X-1	0500880201	D	N_2	–	1.19	5.54E-02	$1899.66^{+490.38}_{-434.10}$	$5.04^{+0.35}_{-0.45}$	$1.42^{+0.04}_{-0.03}$	–	–	–
Cygnus X-1	0500880201	Q	N_1	–	1.46	3.73E-04	$2679.69^{+676.00}_{-600.04}$	0.71	1.55	4.63	–	–
Cygnus X-1	0610000401	Q	TN_4	–	1.13	1.43E-01	$3840.30^{+977.45}_{-868.00}$	$6.18^{+1.11}_{-0.07}$	$1.60^{+0.03}_{-0.01}$	$0.57^{+0.02}_{-0.01}$	–	–
AX J1749.1-2733	0510010401	Q	T_5	–	0.92	6.80E-01	$290.03^{+156.80}_{-119.53}$	$22.81^{+2.70}_{-2.25}$	–	$2.26^{+0.18}_{-0.16}$	–	–
AX J1749.1-2733	0510010401	Q	N_1	–	0.95	6.06E-01	$293.29^{+156.74}_{-121.29}$	$31.98^{+3.03}_{-2.53}$	$1.32^{+0.18}_{-0.16}$	–	–	–

Table A.3. FeKα parameters.

Source	Obs ID	State	P_0	Narrow FeKα					Broad Fe feature				
				Energy (keV)	Width (eV)	$L_{\mathrm{FeK}\alpha}$ (10^{41} γ/s)	EW (keV)	Signif. (σ)	Energy (keV)	Width (eV)	$L_{\mathrm{FeK}\alpha}$ (10^{41} γ/s)	EW (keV)	Signif. (σ)
1A 0535+26	0674180101	Q	8.70E-01	–	–	<6.92$E-02$	<0.06	–	–	–	–	–	–
2S 1845-024	0302970801	Q	7.67E-01	–	–	<1.22$E+00$	<0.60	–	–	–	–	–	–
X Persei	0151380101	Q	3.68E-03	–	–	<2.11$E-01$	<0.03	–	–	–	–	–	–
X Persei	0600980101	Q	1.06E-02	–	–	<1.76$E-01$	<0.02	–	–	–	–	–	–
AX J1820.5-1434	0511010101	Q	9.92E-01	–	–	<4.03$E-01$	<0.21	–	–	–	–	–	–
RX J0146.9+6121	0201160101	Q	8.58E-03	–	–	<4.25$E-02$	<0.06	–	–	–	–	–	–
RX J0440.9+4431	0653660101	Q	8.55E-02	–	–	<4.73$E-01$	<0.06	–	–	–	–	–	–
RX J1037.5-5647	0550560101	Q	4.16E-01	–	–	<1.72$E-01$	<0.13	–	–	–	–	–	–
SAX J2103.5+4545	0149550401	Q	1.77E-02	$6.42^{+0.06}_{-0.04}$	54.00	$3.87E+00^{+3.80E+00}_{-2.59E+00}$	$0.04^{+0.01}_{-0.01}$	3.27	–	–	–	–	–
Swift J045106.8-694803	0679381401	Q	3.28E-01	–	–	<1.80$E+01$	<0.20	–	–	–	–	–	–
V0332+53	0506190101	Q	7.58E-01	–	–	<1.14$E-01$	<2223.78	–	–	–	–	–	–
4U 1538-522	0152780201	EC	7.12E-03	$6.38^{+0.02}_{-0.01}$	0.00	$9.58E-01^{+5.48E-01}_{-3.93E-01}$	$0.18^{+0.04}_{-0.04}$	8.70	$6.54^{+0.02}_{-0.02}$	$271.65^{+20.73}_{-18.92}$	$3.15E+00^{+1.41E+00}_{-1.10E+00}$	$0.92^{+0.14}_{-0.13}$	19.95
4U 1538-522	0152780201	I/E	5.65E-04	$6.40^{+0.01}_{-0.03}$	24.24	$3.42E+00^{+4.16E+00}_{-1.58E+00}$	$0.03^{+0.02}_{-0.01}$	6.46	–	–	–	–	–
4U 1700-37	0083280101	D	9.69E-03	–	–	<6.03$E+00$	<0.27	–	–	–	–	–	–
4U 1700-37	0083280101	F	5.73E-01	$6.48^{+0.06}_{-0.16}$	0.02	$6.86E+00^{+4.54E+00}_{-5.30E+00}$	$0.03^{+0.01}_{-0.02}$	3.56	–	–	–	–	–
4U 1700-37	0083280101	Q	1.04E-01	–	–	<1.23$E+01$	<0.13	–	–	–	–	–	–
4U 1700-37	0083280201	F	1.23E-02	$6.45^{+0.01}_{-0.01}$	$90.60^{+11.35}_{-33.19}$	$2.86E+01^{+1.13E+01}_{-1.31E+01}$	$0.11^{+0.00}_{-0.03}$	19.07	–	–	–	–	–
4U 1700-37	0083280201	Q	7.98E-01	$6.44^{+0.04}_{-0.04}$	$125.45^{+48.71}_{-49.29}$	$9.07E+00^{+5.72E+00}_{-4.56E+00}$	$0.11^{+0.02}_{-0.03}$	7.25	–	–	–	–	–
4U 1700-37	0083280301	Q	1.20E-01	$6.45^{+0.03}_{-0.03}$	$87.78^{+72.25}_{-46.84}$	$8.08E+00^{+6.26E+00}_{-3.82E+00}$	$0.07^{+0.02}_{-0.02}$	8.15	–	–	–	–	–
4U 1700-37	0083280401	EC	1.30E-01	$6.49^{+0.02}_{-0.02}$	$112.97^{+23.82}_{-25.76}$	$3.54E+00^{+1.80E+00}_{-1.45E+00}$	$1.25^{+0.27}_{-0.28}$	12.50	–	–	–	–	–
4U 1700-37	0083280401	I/E	2.01E-01	$6.48^{+0.04}_{-0.03}$	0.00	$7.28E+00^{+3.73E+00}_{-3.67E+00}$	$0.13^{+0.01}_{-0.04}$	6.82	–	–	–	–	–
4U 1700-37	0600950101	EC	6.97E-02	$6.40^{+0.00}_{-0.00}$	$38.57^{+4.33}_{-4.67}$	$2.47E+00^{+9.42E-01}_{-7.77E-01}$	$0.92^{+0.05}_{-0.04}$	>25.5	$6.54^{+0.04}_{-0.03}$	$470.98^{+47.86}_{-35.92}$	$1.07E+00^{+4.84E-01}_{-3.69E-01}$	$0.19^{+0.02}_{-0.01}$	21.33
4U 1907+09	0555410101	F	1.89E-01	$6.43^{+0.03}_{-0.02}$	34.05	$6.04E+00^{+1.10E+00}_{-1.59E+00}$	$0.04^{+0.01}_{-0.01}$	8.55	–	–	–	–	–
4U 1907+09	0555410101	Q	5.16E-01	$6.43^{+0.02}_{-0.02}$	$56.22^{+27.09}_{-46.41}$	$5.29E+00^{+7.56E-01}_{-8.56E-01}$	$0.05^{+0.01}_{-0.01}$	11.60	–	–	–	–	–
EXO1722-363	0206380401	Q	9.84E-03	$6.40^{+0.01}_{-0.01}$	46.25	$1.80E+01^{+1.67E+01}_{-1.09E+01}$	$0.15^{+0.02}_{-0.03}$	13.19	–	–	–	–	–
EXO1722-363	0405640201	EC	7.47E-01	$6.41^{+0.05}_{-0.03}$	$124.04^{+55.59}_{-39.53}$	$1.02E+00^{+1.23E+00}_{-6.50E-01}$	$2.49^{+0.71}_{-0.59}$	7.92	–	–	–	–	–
EXO1722-363	0405640301	Q	7.42E-01	$6.42^{+0.02}_{-0.02}$	54.05	$1.36E+01^{+1.44E+01}_{-8.66E+00}$	$0.14^{+0.03}_{-0.03}$	8.99	–	–	–	–	–
EXO1722-363	0405640401	Q	2.69E-01	$6.41^{+0.01}_{-0.01}$	$45.19^{+20.89}_{-43.01}$	$1.46E+01^{+1.33E+01}_{-8.60E+00}$	$0.23^{+0.03}_{-0.04}$	14.26	–	–	–	–	–
EXO1722-363	0405640901	Q	1.50E-01	$6.42^{+0.72}_{-0.48}$	17.75	$2.99E+00^{+7.11E+01}_{-1.81E+00}$	$0.05^{+0.66}_{-0.01}$	4.02	–	–	–	–	–
EXO1722-363	0405640801	Q	1.44E-01	$6.43^{+0.01}_{-0.01}$	$50.70^{+23.37}_{-37.21}$	$1.57E+01^{+1.49E+01}_{-9.36E+00}$	$0.17^{+0.03}_{-0.03}$	14.20	–	–	–	–	–
GX 301-2	0555200401	F	1.21E-02	$6.37^{+0.00}_{-0.00}$	$25.43^{+1.57}_{-6.61}$	$2.79E+02^{+1.05E+00}_{-7.95E+00}$	$0.46^{+0.00}_{-0.02}$	>25.5	–	–	–	–	–
GX 301-2	0555200401	Q	9.70E-09	$6.38^{+0.01}_{-0.01}$	0.14	$1.41E+02^{+4.70E+00}_{-3.54E+00}$	$0.44^{+0.03}_{-0.02}$	>25.5	–	–	–	–	–
IGR J16207-5129	0402920201	Q	8.16E-02	$6.42^{+0.06}_{-0.05}$	0.00	$4.19E-01^{+3.09E-01}_{-1.77E-01}$	$0.03^{+0.02}_{-0.01}$	2.71	–	–	–	–	–
IGR J16318-4848	0154750401	Q	2.31E-01	$6.40^{+0.00}_{-0.00}$	$35.48^{+6.79}_{-7.68}$	$2.55E+02^{+8.46E+02}_{-2.39E+02}$	$2.47^{+0.25}_{-0.21}$	>25.5	–	–	–	–	–

Notes. Fit parameters of FeKα and broad Fe feature detected. We present the centroid energy (keV), the width (eV), the luminosity (photons/s), EW (keV) and the statistical significance of the Gaussian lines. In the cases where we do not detect FeKα ($\sigma_{\mathrm{sign}} < 2$), we give the upper limits of EW and the luminosity. Parameters frozen or unbounded are included without an error estimation. Therefore they are not used in the plots and the subsequent discussion. The possible states are: quiescence(Q), flare(F), eclipse ingress/egress(I/E), eclipse(E) and dip(D).

Table A.3. continued.

Source	Obs ID	State	P_0	Narrow FeKα					Broad Fe feature				
				Energy (keV)	Width (eV)	$L_{\mathrm{FeK}\alpha}$ (10^{41} γ/s)	EW (keV)	Signif. (σ)	Energy (keV)	Width (eV)	$L_{\mathrm{FeK}\alpha}$ (10^{41} γ/s)	EW (keV)	Signif. (σ)
IGR J16318-4848	0201000201	Q	7.12E-01	$6.41^{+0.01}_{-0.01}$	26.59	$1.05E+02^{+3.07E+02}_{-9.88E+01}$	$1.12^{+0.13}_{-0.13}$	>25.5	–	–	–	–	–
IGR J16318-4848	0201000301	Q	6.83E-01	$6.42^{+0.02}_{-0.01}$	32.52	$3.96E+02^{+2.58E+03}_{-3.88E+02}$	$2.28^{+1.47}_{-0.68}$	10.97	–	–	–	–	–
IGR J16318-4848	0201000401	Q	2.57E-01	$6.41^{+0.01}_{-0.01}$	27.11	$4.56E+01^{+1.51E+02}_{-4.31E+01}$	$1.15^{+0.15}_{-0.16}$	22.68	–	–	–	–	–
IGR J16320-4751	0128531101	Q	4.94E-01	–	–	<3.78E+00	<0.28	–	–	–	–	–	–
IGR J16320-4751	0201700301	F	8.13E-01	$6.41^{+0.02}_{-0.01}$	31.55	$1.92E+01^{+1.84E+01}_{-1.17E+01}$	$0.13^{+0.01}_{-0.02}$	5.38	–	–	–	–	–
IGR J16320-4751	0201700301	Q	6.96E-01	$6.42^{+0.00}_{-0.01}$	0.00	$7.80E+00^{+7.17E+00}_{-4.60E+00}$	$0.11^{+0.01}_{-0.01}$	9.58	–	–	–	–	–
IGR J16320-4751	0556140101	Q	5.15E-01	$6.44^{+0.03}_{-0.07}$	0.00	$1.83E+01^{+1.62E+01}_{-1.67E+01}$	$0.22^{+0.01}_{-0.19}$	15.57	–	–	–	–	–
IGR J16320-4751	0556140201	Q	3.47E-01	$6.42^{+0.01}_{-0.01}$	26.65	$2.92E+01^{+2.56E+01}_{-1.80E+01}$	$0.19^{+0.01}_{-0.03}$	6.60	–	–	–	–	–
IGR J16320-4751	0556140301	Q	2.28E-01	$6.42^{+0.01}_{-0.01}$	0.00	$2.23E+01^{+2.17E+01}_{-1.39E+01}$	$0.15^{+0.02}_{-0.03}$	5.52	–	–	–	–	–
IGR J16320-4751	0556140401	Q	6.25E-02	$6.43^{+0.01}_{-0.02}$	$68.31^{+19.44}_{-23.31}$	$1.64E+01^{+1.60E+01}_{-9.98E+00}$	$0.17^{+0.02}_{-0.02}$	17.17	–	–	–	–	–
IGR J16320-4751	0556140501	Q	8.57E-01	$6.41^{+0.02}_{-0.02}$	0.00	$1.13E+01^{+1.27E+01}_{-7.30E+00}$	$0.15^{+0.03}_{-0.03}$	7.71	–	–	–	–	–
IGR J16320-4751	0556140601	Q	3.73E-01	$6.42^{+0.01}_{-0.01}$	$34.48^{+11.53}_{-31.19}$	$3.72E+01^{+3.25E+01}_{-2.29E+01}$	$0.20^{+0.01}_{-0.04}$	15.70	–	–	–	–	–
IGR J16320-4751	0556140701	Q	5.34E-02	$6.42^{+0.01}_{-0.01}$	$45.43^{+8.55}_{-29.65}$	$2.83E+01^{+2.46E+01}_{-1.77E+01}$	$0.41^{+0.04}_{-0.09}$	10.46	–	–	–	–	–
IGR J16320-4751	0556140801	Q	1.31E-01	$6.42^{+0.01}_{-0.01}$	$52.95^{+20.85}_{-29.37}$	$1.67E+01^{+1.61E+01}_{-1.01E+01}$	$0.19^{+0.02}_{-0.02}$	19.00	–	–	–	–	–
IGR J16320-4751	0556141001	Q	7.05E-01	$6.42^{+0.01}_{-0.01}$	21.72	$1.72E+01^{+1.82E+01}_{-1.05E+01}$	$0.15^{+0.03}_{-0.02}$	8.66	–	–	–	–	–
IGR J16465-4507	0164561001	Q	9.23E-01	–	–	<5.27E+00	<0.50	–	–	–	–	–	–
SAX J1802.7-2017	0206380601	Q	3.18E-02	–	–	<1.36E+01	<0.14	–	–	–	–	–	–
Vela X-1	0111030101	F	4.24E-03	$6.45^{+0.02}_{-0.02}$	55.91	$7.27E+00^{+3.78E+00}_{-2.56E+00}$	$0.07^{+0.02}_{-0.01}$	9.75	–	–	–	–	–
Vela X-1	0111030101	Q	8.65E-01	$6.45^{+0.01}_{-0.01}$	$45.04^{+18.62}_{-25.41}$	$4.00E+00^{+1.50E+00}_{-1.15E+00}$	$0.06^{+0.01}_{-0.01}$	19.86	$6.62^{+0.08}_{-0.11}$	$1220.66^{+115.79}_{-76.84}$	$4.29E+01^{+1.91E+01}_{-1.24E+01}$	$0.75^{+0.15}_{-0.09}$	>25.5
XTE J0421+560	0139760101	Q	9.51E-01	$6.43^{+0.03}_{-0.03}$	0.00	$2.78E-01^{+1.61E+00}_{-2.69E-01}$	$0.15^{+0.21}_{-0.04}$	2.65	$6.56^{+0.21}_{-2.68}$	$402.38^{+4955.35}_{-58.40}$	$7.08E-01^{+2.67E+01}_{-6.86E-01}$	$0.43^{+4.28}_{-0.13}$	3.51
AXJ1841.0-0536	0604820301	F	1.54E-03	$6.46^{+0.07}_{-0.06}$	0.00	$1.67E+00^{+1.18E+00}_{-1.19E+00}$	$0.02^{+0.01}_{-0.01}$	2.78	–	–	–	–	–
IGR J00370+6122	0501450101	Q	9.23E-01	–	–	<2.97E-01	<0.06	–	–	–	–	–	–
IGR J11215-5952	0405181901	F	3.64E-01	$6.48^{+0.04}_{-0.05}$	$62.01^{+52.30}_{-45.59}$	$4.16E+00^{+1.38E+00}_{-1.45E+00}$	$0.05^{+0.02}_{-0.02}$	3.49	–	–	–	–	–
IGR J11215-5952	0405181901	Q	5.39E-01	–	–	<1.16E+00	<0.13	–	–	–	–	–	–
IGR J16328-4726	0654190201	Q	3.77E-01	–	–	<4.94E-01	<0.09	–	–	–	–	–	–
IGR J16418-4532	0206380301	Q	7.30E-01	–	–	<1.34E+00	<0.07	–	–	–	–	–	–
IGR J16418-4532	0405180501	Q	1.99E-01	–	–	<6.39E-01	<0.05	–	–	–	–	–	–
IGRJ16479-4514	0512180101	EC	5.92E-01	$6.42^{+0.02}_{-0.00}$	0.00	$4.89E-01^{+5.75E-01}_{-3.34E-01}$	$0.45^{+0.11}_{-0.14}$	6.36	–	–	–	–	–
IGRJ16479-4514	0512180101	I/E	9.67E-01	6.40	0.00	1.72E+00	0.03	1.48	–	–	–	–	–
XTE J1739-302	0554720101	F	5.66E-02	–	–	<3.81E-02	<0.21	–	–	–	–	–	–
XTE J1739-302	0554720101	Q	2.51E-01	–	–	<1.83E-02	<2.27	–	–	–	–	–	–
XTE J1739-302	0561580101	F	6.04E-01	–	–	<9.58E-02	<0.12	–	–	–	–	–	–
XTE J1739-302	0561580101	Q	6.93E-02	–	–	<2.35E-02	<0.17	–	–	–	–	–	–
IGR J17544-2619	0148090501	F	7.16E-01	–	–	<2.39E-01	<0.12	–	–	–	–	–	–
IGR J18450-0435	0306170401	F	3.51E-01	–	–	<2.24E+00	<0.13	–	–	–	–	–	–
IGR J18450-0435	0306170401	Q	3.39E-01	–	–	<4.27E-01	<0.14	–	–	–	–	–	–

Table A.3. continued.

Source	Obs ID	State	P_0	Narrow FeKα					Broad Fe feature				
				Energy (keV)	Width (eV)	$L_{\mathrm{FeK}\alpha}$ (10^{41} γ/s)	EW (keV)	Signif. (σ)	Energy (keV)	Width (eV)	$L_{\mathrm{FeK}\alpha}$ (10^{41} γ/s)	EW (keV)	Signif. (σ)
IGR J18483-0311	0406140201	Q	1.98E-01	–	–	$<4.23E-02$	<0.27	–	–	–	–	–	–
γ Cassiopeiae	0201220101	Q	1.42E-03	$6.43^{+0.01}_{-0.01}$	0.00	$6.86E-04^{+2.62E-04}_{-1.95E-04}$	$0.03^{+0.00}_{-0.00}$	13.80	–	–	–	–	–
γ Cassiopeiae	0651670201	Q	3.62E-02	$6.39^{+0.03}_{-0.02}$	23.94	$1.08E-03^{+5.03E-04}_{-4.24E-04}$	$0.04^{+0.01}_{-0.01}$	7.82	–	–	–	–	–
γ Cassiopeiae	0651670301	Q	4.40E-04	$6.44^{+0.26}_{-0.03}$	6.39	$1.00E-03^{+2.86E-03}_{-3.77E-04}$	$0.04^{+0.11}_{-0.01}$	7.41	–	–	–	–	–
γ Cassiopeiae	0651670401	Q	1.09E-01	$6.41^{+0.02}_{-0.02}$	1.50	$1.53E-03^{+6.94E-04}_{-4.17E-04}$	$0.05^{+0.01}_{-0.00}$	10.26	–	–	–	–	–
γ Cassiopeiae	0651670501	Q	6.73E-02	$6.39^{+0.02}_{-0.03}$	0.00	$8.55E-04^{+3.70E-04}_{-3.18E-04}$	$0.04^{+0.01}_{-0.01}$	7.91	–	–	–	–	–
HD 110432	0504730101	Q	2.81E-02	$6.44^{+0.03}_{-0.04}$	0.14	$1.21E-03^{+7.92E-04}_{-5.97E-04}$	$0.05^{+0.01}_{-0.02}$	5.36	–	–	–	–	–
HD 119682	0551000201	Q	2.06E-01	–	–	$<7.53E-03$	<0.63	–	–	–	–	–	–
HD 157832	0551020101	Q	3.12E-01	6.40	0.00	$1.32E-03^{+8.17E-04}_{-9.18E-04}$	$0.10^{+0.06}_{-0.07}$	2.47	–	–	–	–	–
HD 161103	0201200101	Q	9.76E-02	6.40	0.00	$4.68E-03^{+9.96E-03}_{-4.19E-03}$	$0.09^{+0.07}_{-0.07}$	2.18	–	–	–	–	–
HD 45314	0670080301	Q	5.63E-01	$6.39^{+2.77}_{-0.65}$	0.00	$5.45E-03$	0.17	1.98	–	–	–	–	–
SAO 49725	0201200201	Q	7.39E-02	–	–	$<3.26E-02$	<0.71	–	–	–	–	–	–
SS397	0122700101	Q	7.90E-01	–	–	$<1.00E-02$	<0.42	–	–	–	–	–	–
SS397	0122700201	Q	6.88E-01	–	–	$<1.00E-02$	<0.43	–	–	–	–	–	–
SS397	0122700301	Q	4.21E-01	–	–	$<1.10E-02$	<0.57	–	–	–	–	–	–
SS397	0122700501	Q	4.49E-01	–	–	$<2.69E-02$	<1.31	–	–	–	–	–	–
LS I +61 303	0207260101	Q	2.25E-01	–	–	$<2.16E-02$	<0.04	–	–	–	–	–	–
LS I +61 303	0505980801	Q	4.04E-01	–	–	$<5.80E-02$	<0.12	–	–	–	–	–	–
LS I +61 303	0505980901	Q	8.86E-02	–	–	$<8.59E-02$	<0.14	–	–	–	–	–	–
LS I +61 303	0505981001	Q	2.44E-01	–	–	$<9.20E-02$	<0.17	–	–	–	–	–	–
LS I +61 303	0505981101	Q	7.24E-01	–	–	$<4.72E-02$	<0.08	–	–	–	–	–	–
LS I +61 303	0505981201	Q	5.09E-01	–	–	$<1.16E-01$	<0.10	–	–	–	–	–	–
LS I +61 303	0505981301	Q	3.03E-01	–	–	$<5.54E-02$	<0.06	–	–	–	–	–	–
LS I +61 303	0505981401	Q	1.03E-01	–	–	$<6.98E-02$	<0.12	–	–	–	–	–	–
LS 5039	0151160201	Q	9.13E-02	–	–	$<4.72E-02$	<0.10	–	–	–	–	–	–
LS 5039	0151160301	Q	6.01E-02	–	–	$<1.06E-01$	<0.22	–	–	–	–	–	–
LS 5039	0202950201	Q	1.14E-01	–	–	$<4.72E-02$	<0.08	–	–	–	–	–	–
LS 5039	0202950301	Q	8.41E-02	–	–	$<8.39E-02$	<0.28	–	–	–	–	–	–
4U 2206+54	0650640101	Q	5.04E-02	–	–	$<1.21E+00$	<0.03	–	–	–	–	–	–
Cen X-3	0111010101	I/E	1.24E-02	$6.41^{+0.01}_{-0.01}$	$42.06^{+17.30}_{-13.71}$	$5.77E+01^{+2.06E+01}_{-1.45E+01}$	$0.14^{+0.02}_{-0.01}$	16.08	–	–	–	–	–
Cygnus X-1	0202401101	Q	1.54E-01	$6.59^{+0.05}_{-0.04}$	0.00	$6.22E+00^{+4.51E+00}_{-3.50E+00}$	$0.01^{+0.01}_{-0.01}$	3.46	$6.42^{+0.06}_{-0.09}$	$873.82^{+100.30}_{-110.40}$	$1.66E+02^{+8.33E+01}_{-4.86E+01}$	$0.44^{+0.09}_{-0.06}$	18.93
Cygnus X-1	0202401201	Q	1.39E-01	–	–	–	–	–	$6.50^{+0.07}_{-0.09}$	$944.58^{+156.75}_{-84.66}$	$1.31E+02^{+7.54E+01}_{-4.24E+01}$	$0.46^{+0.13}_{-0.06}$	19.49
Cygnus X-1	0202760201	Q	2.94E-03	$6.55^{+0.01}_{-0.02}$	0.00	$1.07E+01^{+4.57E+00}_{-3.49E+00}$	$0.01^{+0.00}_{-0.00}$	5.82	$6.55^{+0.02}_{-0.03}$	$1101.52^{+54.39}_{-35.58}$	$4.82E+02^{+1.80E+02}_{-1.26E+02}$	$0.65^{+0.07}_{-0.04}$	5.82
Cygnus X-1	0202760301	Q	5.82E-01	$6.54^{+0.02}_{-0.02}$	0.00	$5.54E+00^{+2.72E+00}_{-2.11E+00}$	$0.01^{+0.00}_{-0.00}$	7.72	$6.41^{+0.04}_{-0.04}$	$1243.17^{+66.00}_{-52.76}$	$3.29E+02^{+1.19E+02}_{-9.09E+01}$	$0.61^{+0.05}_{-0.04}$	>25.5
Cygnus X-1	0202760401	Q	6.18E-05	$6.48^{+0.03}_{-0.01}$	0.00	$6.01E+00^{+3.04E+00}_{-2.43E+00}$	$0.01^{+0.00}_{-0.00}$	7.47	$6.47^{+0.03}_{-0.03}$	$1199.67^{+57.79}_{-37.68}$	$4.64E+02^{+1.65E+02}_{-1.18E+02}$	$0.61^{+0.06}_{-0.02}$	4.02
Cygnus X-1	0202760501	Q	1.38E-01	$6.53^{+0.02}_{-0.02}$	0.00	$1.12E+01^{+5.53E+00}_{-3.99E+00}$	$0.01^{+0.00}_{-0.00}$	8.97	$6.46^{+0.03}_{-0.06}$	$1297.32^{+91.10}_{-52.59}$	$6.03E+02^{+2.45E+02}_{-1.67E+02}$	$0.83^{+0.11}_{-0.06}$	>25.5

Table A.3. continued.

Source	Obs ID	State	P_0	Narrow FeKα					Broad Fe feature				
				Energy (keV)	Width (eV)	$L_{\mathrm{FeK}\alpha}$ (10^{41} γ/s)	EW (keV)	Signif. (σ)	Energy (keV)	Width (eV)	$L_{\mathrm{FeK}\alpha}$ (10^{41} γ/s)	EW (keV)	Signif. (σ)
Cygnus X-1	0500880201	D	6.15E-02	–	–	–	–	–	$6.36^{+0.21}_{-0.22}$	$595.01^{+365.26}_{-181.09}$	$2.13E+01^{+1.59E+01}_{-1.10E+01}$	$0.09^{+0.03}_{-0.03}$	4.99
Cygnus X-1	0500880201	Q	3.73E-04	6.41	0.00	$4.94E+00^{+1.25E+00}_{-1.11E+00}$	0.02	6.95	–	–	–	–	–
Cygnus X-1	0610000401	Q	1.43E-01	$6.46^{+0.03}_{-0.09}$	$82.68^{+142.20}_{-34.87}$	$7.05E+00^{+6.63E+00}_{-2.98E+00}$	$0.02^{+0.01}_{-0.01}$	5.09	–	–	–	–	–
AX J1749.1-2733	0510010401	Q	6.80E-01	–	–	<6.11E+00	<0.12	–	–	–	–	–	–

Appendix B: Spectral atlas

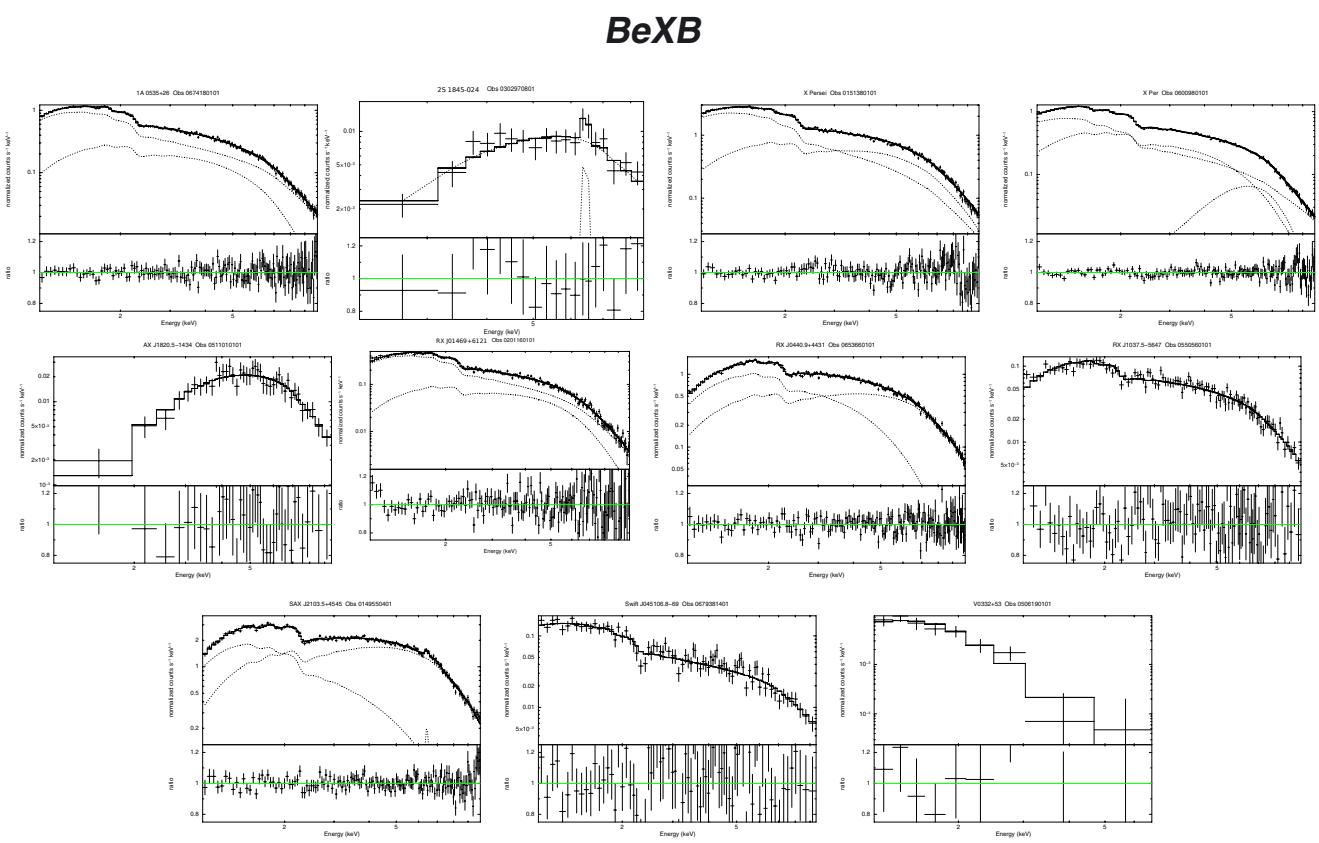

Fig. B.1. BeXBs data, model, model components and ratio data/model. The spectra are typically soft, with no Fe emission lines.

SGXB

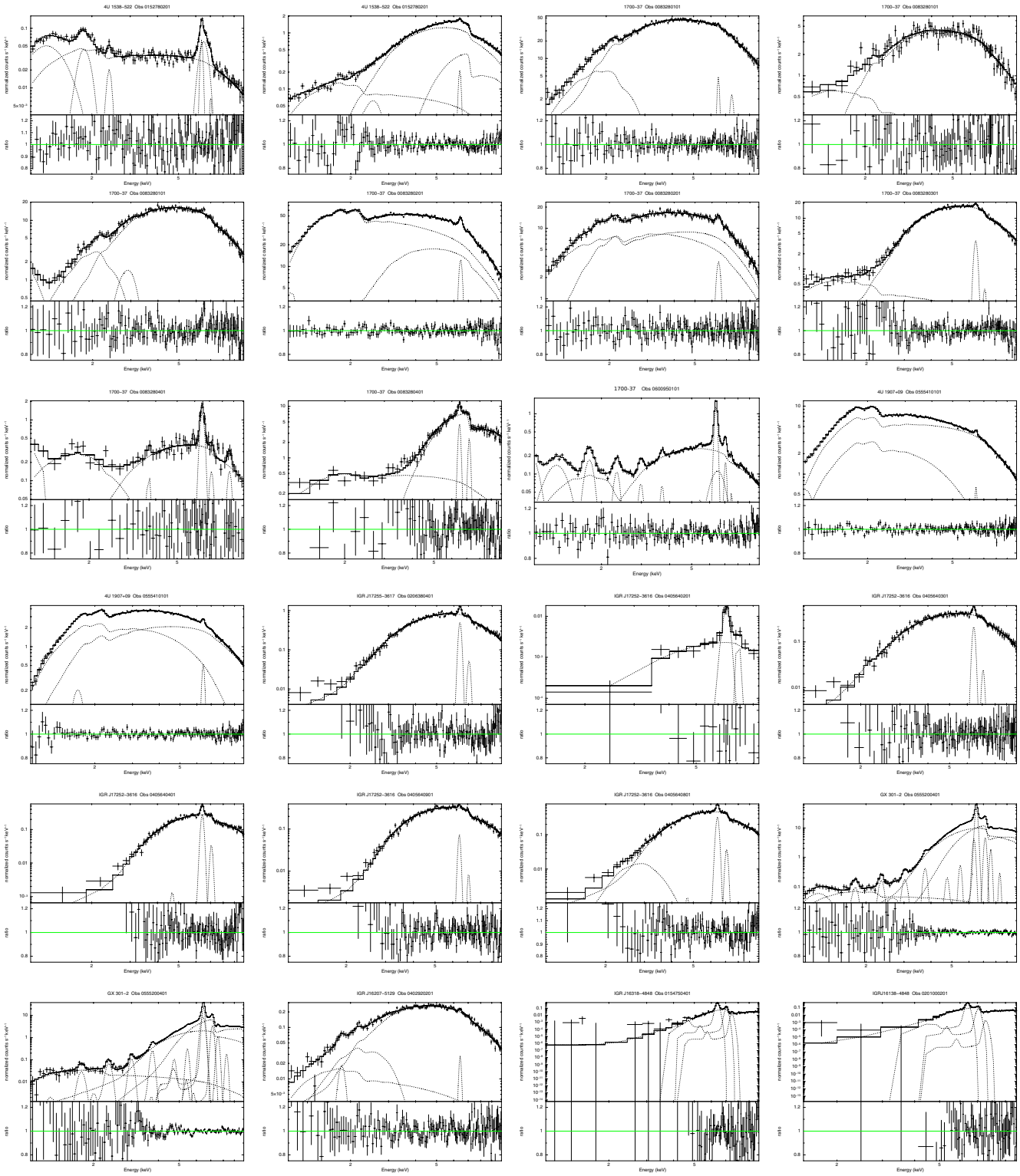

Fig. B.2. SGXBs data, model, model components and ratio data/model. The spectra are characteristically affected by high absorption, with Fe fluorescent lines.

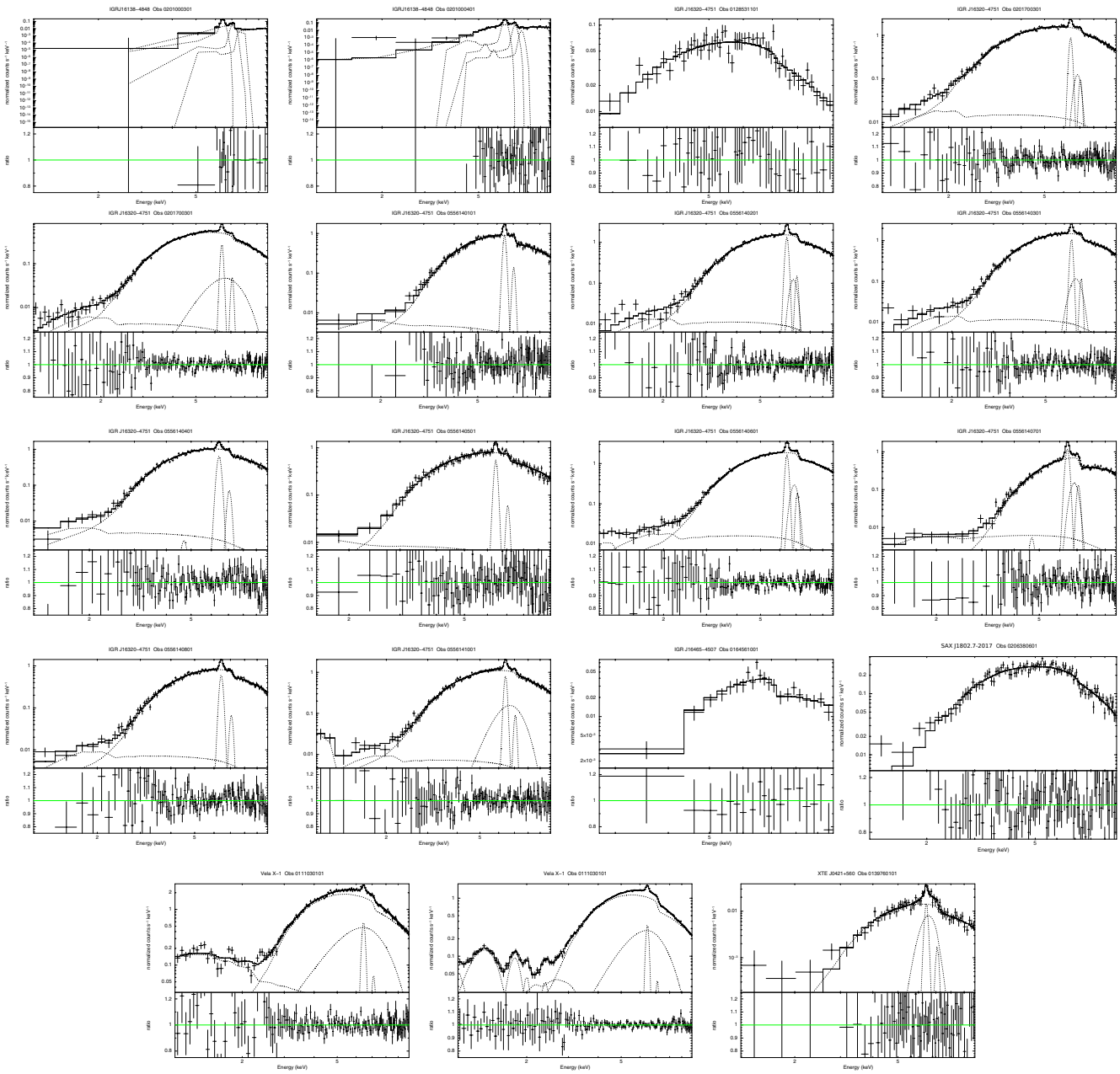

Fig. B.2. continued.

SFXT

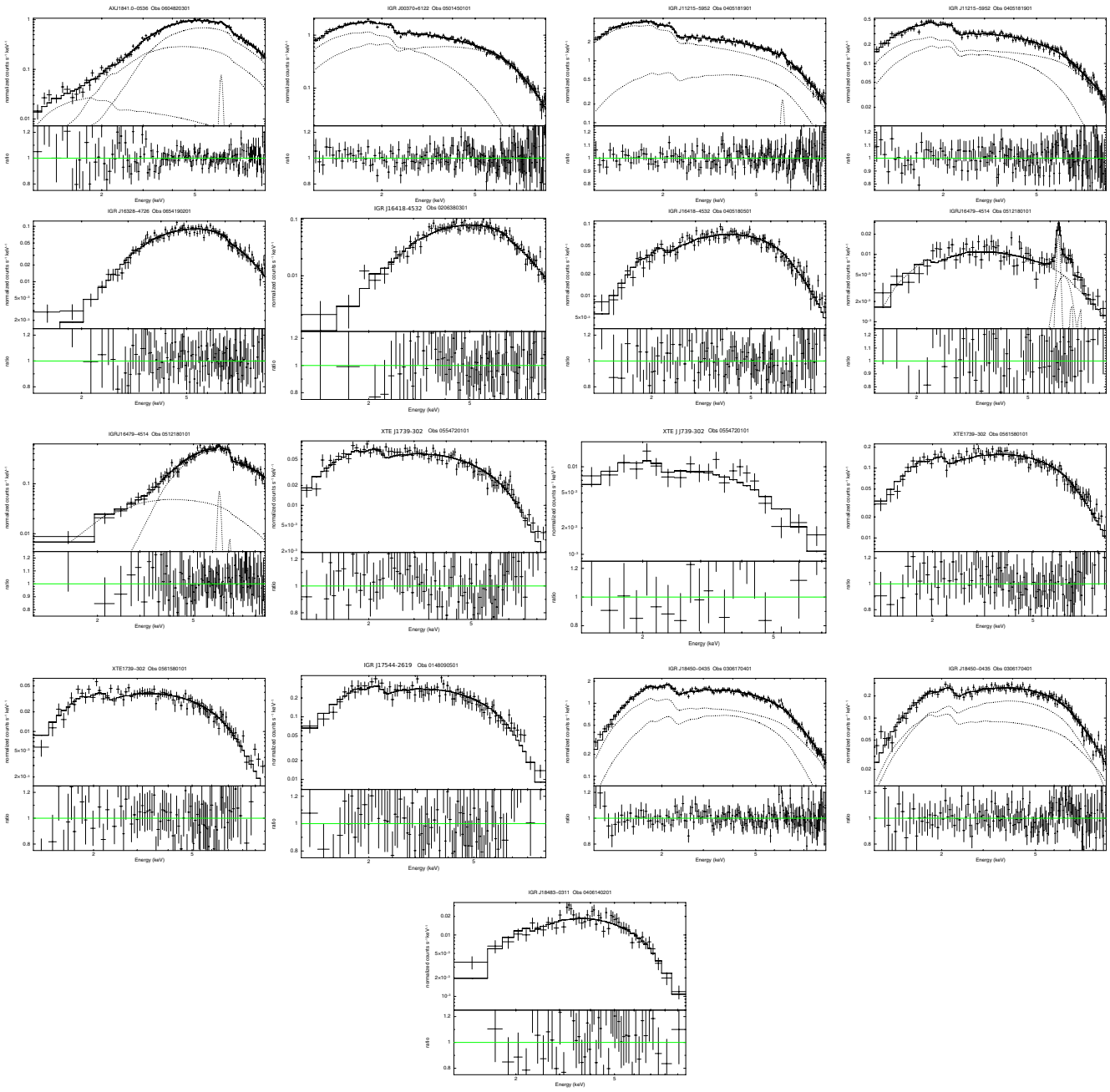

Fig. B.3. SFXTs data, model, model components and ratio data/model.

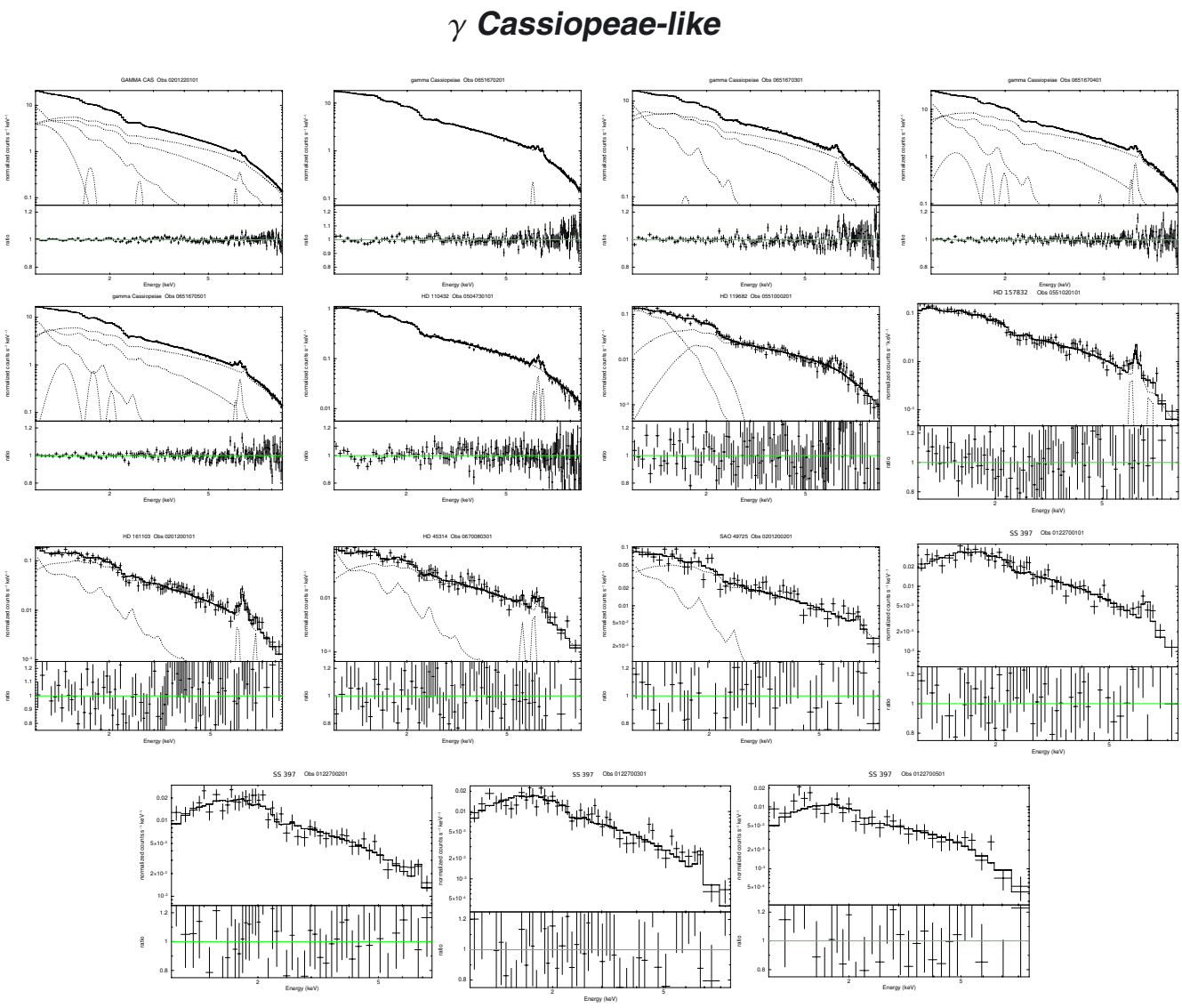

Fig. B.4. γ Cass-like systems data, model, model components and ratio data/model. The data is usually fitted using thermal models, including Fe recombination lines. FeKα is also usually visible.

HMGB

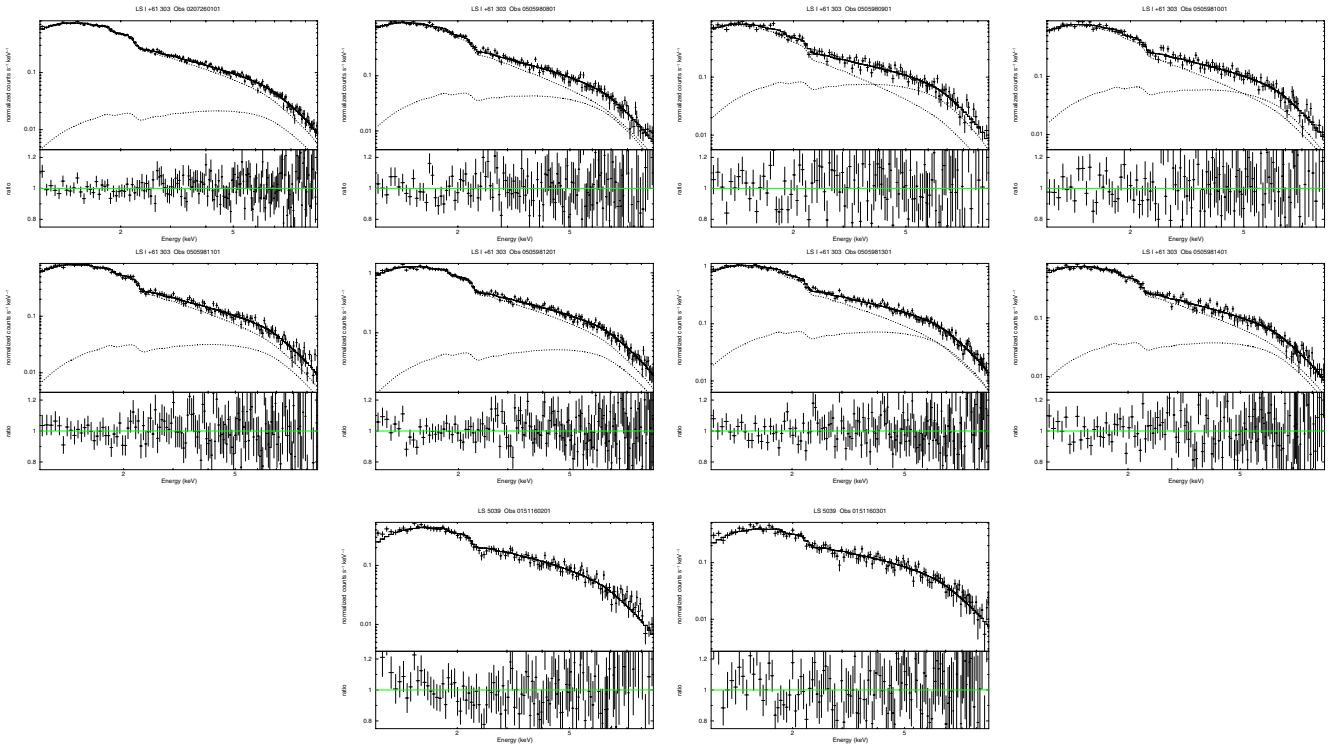

Fig. B.5. HMGBs data, model, model components and ratio data/model. Soft spectra with no sign of Fe lines.

Unclassified

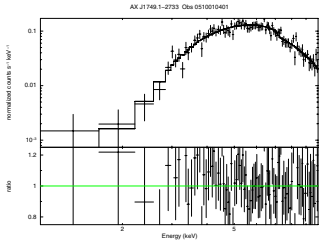

Fig. B.6. AX J1749.1-2733 data, model, model components, and ratio data/model. We have no references for the luminosity class of the optical star, although the high absorption we observed points to a supergiant companion.

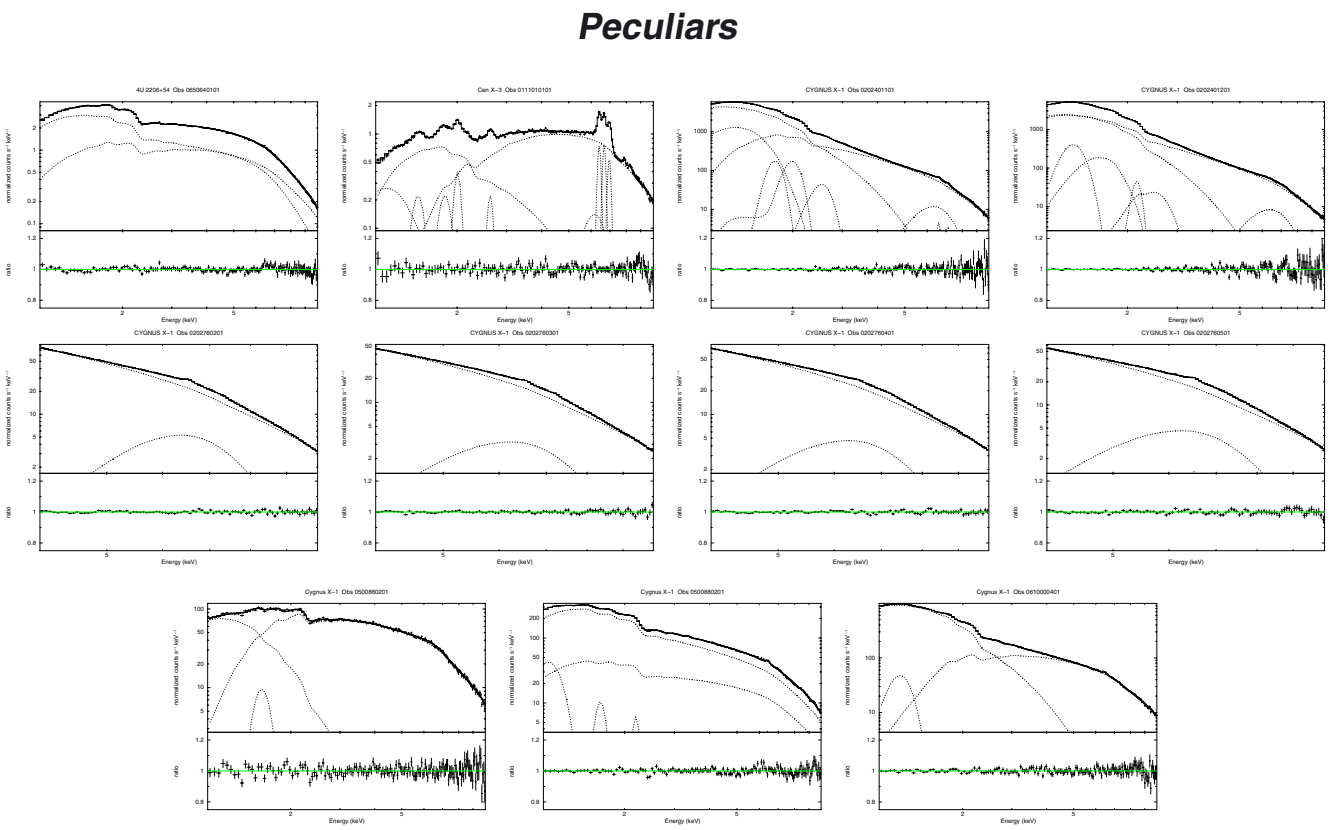

Fig. B.7. Peculiar sources data, model, model components and ratio data/model. These sources can hardly be categorized in any of the described HMXBs standard groups.